Detailed Oscillation Analysis and Parameter Selection Principle for Boost PFC Converter With *RC* Snubber Operated in DCM

Kai Yao, *Member, IEEE*, Hairui Xu, Qiang Li, Yehua Han, and Ke Yun

***Abstract*—The parasitic parameters of a boost power factor correction converter lead to input current distortion when the converter operates in discontinuous conduction mode, and using an *RC* snubber is a simple and effective way to suppress the parasitic oscillation. The effect of the *RC* snubber on the parasitic oscillation is analyzed in detail, and three different forms of the characteristic roots are obtained according to different *RC* values. The optimal *RC* values and their relationship between the inductance and parasitic capacitance are figured out, which can achieve a lowest total harmonic distortion. A 1-kW prototype has been built and tested at low power and the experimental waveforms and data are presented to validate the theoretical analysis.**

***Index Terms*—Discontinuous conduction mode (DCM), parasitic oscillation suppression, power factor correction (PFC), *RC* snubber.**

I. Introduction

BOOST power factor correction (PFC) converter has been widely used in power electronic devices because it exhibits several advantages [1]–[10]. Depending on whether the inductor current is continuous or not, a boost PFC converter can be designed to operate in three modes: continuous conduction mode (CCM), critical conduction mode, and discontinuous conduction mode (DCM) [11]–[18].

With the decrease of output power, the inductor current of a CCM boost PFC converter will fall into DCM around 0 and π, and remain in CCM around $\pi/2$ of a half line cycle. When the load lightens to a certain degree, the inductor current will be fully in DCM during $[0, \pi]$. Correspondingly, the control algorithms for CCM are not suitable anymore and a number of improved control strategies have been proposed [19]–[27]. On the other hand, because of the power components, which are originally adopted for CCM, the resultant rich parasitic parameters will cause serious input current distortion [28]–[36].

Manuscript received December 20, 2017; revised February 24, 2018 and May 5, 2018; accepted June 7, 2018. Date of publication June 24, 2018; date of current version February 20, 2019. This work was supported in part by the National Natural Science Foundation of China (51677091), in part by the Excellent Youth Fund Project of Jiangsu Natural Science Foundation (BK20160086), and in part by the Six Talents Peak Project of Jiangsu Province (XNY-033). Recommended for publication by Associate Editor R. Redl. *(Corresponding author: Kai Yao.)*

The authors are with the School of Automation, Nanjing University of Science and Technology, Nanjing 210094, China (e-mail:

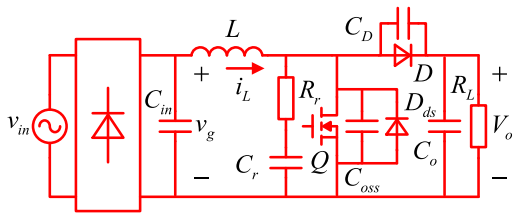

Fig. 1. Boost PFC circuit with parasitic parameters and *RC* snubber.

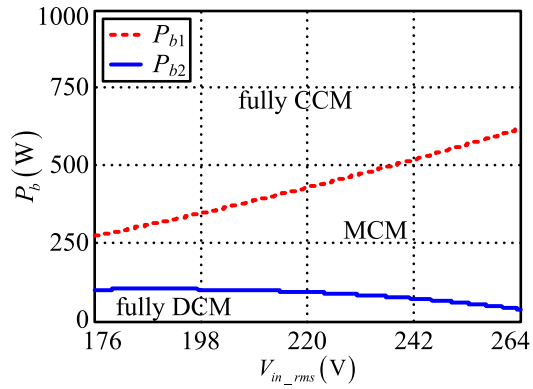

Fig. 2. Curves of critical load power.

freewheeling diode is considered as an ideal one with a junction capacitance C_D in parallel.

In order to facilitate the analysis of the effect of parasitic parameters on the input current, the hypotheses are made as follows: 1) the switching frequency f_s is far greater than the input voltage frequency f_l and the input voltage is approximately constant in a switching cycle; 2) the output voltage ripple is much lower than its dc component V_o.

The input voltage is defined as

$$v_{\text{in}}(n) = V_m \sin(\omega n T_s) \tag{1}$$

where V_m and ω are the amplitude and angular frequency of the input voltage, respectively. T_s is the switching cycle, n is the number of T_s.

Then, the rectified input voltage is

$$v_g(n) = V_m \left|\sin(\omega n T_s)\right|. \tag{2}$$

When a CCM boost PFC converter operates at light loads, the critical load power for completely CCM and fully DCM operation is expressed in P_{b1} and P_{b2}, respectively, as follows [21] and [25]:

$$P_{b1} = \frac{V_m^2}{4Lf_s} \tag{3(a)}$$

$$P_{b2} = \frac{V_m^2(V_o - V_m)}{4Lf_s V_o}. \tag{3(b)}$$

Combining with the circuit parameters given in Section IV, Fig. 2 can be plotted from 3(a) and 3(b), which shows the critical load power corresponding to a certain input voltage, where $V_{\text{in\_rms}}$ is the effective value of the input voltage. Mixed conduction mode (MCM) means that the converter will operate in CCM around $\pi/2$, and DCM around 0 and π, respectively, during half of an input line cycle.

When the inductor current of the DCM boost PFC converter drops to zero, the inductor will oscillate with the parasitic parameters of the circuit. The *RC* snubber consumes the energy stored in the parasitic parameters of the circuit so that the oscillating current drops rapidly to zero, thereby the input current distortion can be reduced. Because the capacitance of C_{in} and C_o is much larger than the parasitic capacitance, they can be regarded as a constant voltage source in the oscillation period. The equivalent circuit in the oscillation period is shown in Fig. 3(a).

The KVL and KCL equations for the circuit are

$$\begin{cases} v_{C_{\text{oss}}}(t) - v_{C_D}(t) = V_o \\ v_{CD}(t) + v_L(t) = v_g(n) - V_o \\ R_r \times i_{\text{RC}}(t) + v_{C_r}(t) = v_{C_{\text{oss}}}(t) \\ i_L(t) = i_{C_D}(t) + i_{C_{\text{oss}}}(t) + i_{\text{RC}}(t) \end{cases} \tag{4}$$

where

$$\begin{cases} v_L(t) = L\dfrac{di_L(t)}{dt} \\ i_{C_{\text{oss}}}(t) = C_{\text{oss}}\dfrac{dv_{C_{\text{oss}}}(t)}{dt} \\ i_{C_D}(t) = C_D\dfrac{dv_{C_D}(t)}{dt} \\ i_{\text{RC}}(t) = C_r\dfrac{dv_{C_r}(t)}{dt}. \end{cases} \tag{5}$$

Based on (4) and (5), the differential equation of the inductor current can be obtained as

$$(C_{\text{oss}} + C_D)C_r R_r L\frac{d^3 i_L}{dt^3} + (C_{\text{oss}} + C_D + C_r)L\frac{d^2 i_L}{dt^2} + C_r R_r \frac{di_L}{dt} + i_L = 0. \tag{6}$$

The characteristic equation of (6) is

$$ar^3 + br^2 + cr + 1 = 0 \tag{7}$$

where

$$\begin{cases} C_{\text{eq}} = C_{\text{oss}} + C_D \\ a = C_{\text{eq}} C_r R_r L \\ b = (C_{\text{eq}} + C_r)L \\ c = C_r R_r. \end{cases} \tag{8}$$

According to [37] and [38], the three characteristic roots of (7) are formulated as

$$\begin{cases} r_1 = -\frac{b}{a} - 2\alpha \\ r_2 = \alpha + \beta i \\ r_3 = \alpha - \beta i \end{cases} \tag{9}$$

where, (10) and (11) as shown at the bottom of the next page.

Furthermore, the characteristic roots have three different forms: a simple root and two multiple roots; a simple root and two complex conjugate roots; and three simple roots.

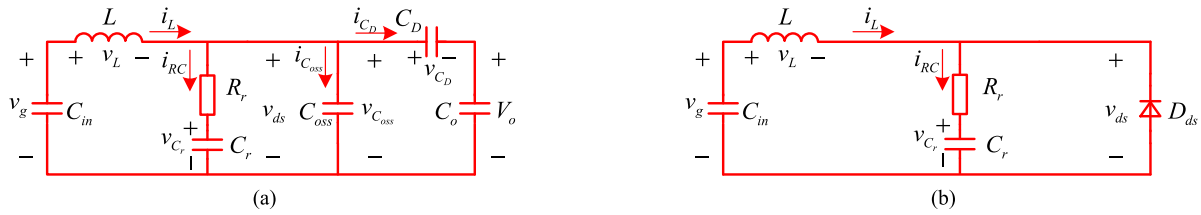

Fig. 3. Equivalent circuits in oscillation period. (a) Parasitic antiparallel diode turns off. (b) Parasitic antiparallel diode turns on.

The complex regime form of (6) can be written as

$$C_{\mathrm{eq}}C_r R_r L s^3 + (C_{\mathrm{eq}} + C_r) L s^2 + C_r R_r s + 1 = 0. \quad (12)$$

Taking the capacitance C_r of snubber as the variable parameter, we can rearrange (12) as

$$1 + C_r \frac{C_{\mathrm{eq}} R_r L s^3 + L s^2 + R_r s}{C_{\mathrm{eq}} L s^2 + 1} = 0. \quad (13)$$

In a root locus diagram, the intersection of root locus and the real axis is called the breakaway point. While the value of C_r increases from zero, the imaginary part of two conjugate complex roots decreases. When the imaginary part of two conjugate complex roots is equal to zero, the two complex conjugate roots coincide at the breakaway point, and (13) has two multiple roots γ less than zero. In addition, γ is also a root of (13)'s derivative being equal to zero [39]. Therefore, the following equations can be written:

$$1 + C_r \frac{C_{\mathrm{eq}} R_r L \gamma^3 + L \gamma^2 + R_r \gamma}{C_{\mathrm{eq}} L \gamma^2 + 1} = 0 \quad (14)$$

$$\frac{d}{\mathrm{ds}} \left(1 + C_r \frac{C_{\mathrm{eq}} R_r L s^3 + L s^2 + R_r s}{C_{\mathrm{eq}} L s^2 + 1} \right) \Bigg|_{s=\gamma} = 0. \quad (15)$$

Through (14) and (15), the expression of R_r and C_r regarding γ is

$$R_r = -\frac{2L\gamma}{\left(C_{\mathrm{eq}} L \gamma^2 + 1\right)^2} \quad (16)$$

$$C_r = -\frac{\left(C_{\mathrm{eq}} L \gamma^2 + 1\right)^2}{C_{\mathrm{eq}} L^2 \gamma^4 - L\gamma^2}. \quad (17)$$

In this paper, the inductance and parasitic capacitance are taken into account for the parasitic parameters, which determine the *RC* values. Therefore, in order to facilitate the analysis, we should establish the relationship between C_r and C_{eq}. See Appendix A, we can get the following expressions:

$$R_{r\_\mathrm{critical1}} = \frac{8(k+1)^2}{\left(3k - \sqrt{k\,(k-8)}\right)^2} \sqrt{\frac{k - 2 - \sqrt{k\,(k-8)}}{2\,(k+1)}}$$

$$\sqrt{\frac{L}{C_{\mathrm{eq}}}} = f_1\,(k) \cdot \sqrt{\frac{L}{C_{\mathrm{eq}}}} \quad (18)$$

$$R_{r\_\mathrm{critical2}} = \frac{8(k+1)^2}{\left(3k + \sqrt{k\,(k-8)}\right)^2} \sqrt{\frac{k - 2 + \sqrt{k\,(k-8)}}{2\,(k+1)}}$$

$$\sqrt{\frac{L}{C_{\mathrm{eq}}}} = f_2\,(k) \cdot \sqrt{\frac{L}{C_{\mathrm{eq}}}}. \quad (19)$$

The curves of $f_1(k)$ and $f_2(k)$ are depicted in Fig. 4, which reveal that $k \geq 8$ should be satisfied in order to obtain real

$$\alpha = -\frac{b}{3a} + \frac{\left(-b^2 + 3ac\right)}{3 \times 2^{2/3} a \left(-27a^2 - 2b^3 + 9abc + \sqrt{4(-b^2+3ac)^3 + (-27a^2 - 2b^3 + 9abc)^2} \right)^{1/3}}$$
$$- \frac{\left(-27a^2 - 2b^3 + 9abc + \sqrt{4(-b^2+3ac)^3 + (-27a^2 - 2b^3 + 9abc)^2} \right)^{1/3}}{6 \times 2^{1/3} a} \quad (10)$$

$$\beta = \frac{\sqrt{3}\left(-b^2 + 3ac\right)}{3 \times 2^{2/3} a \left(-27a^2 - 2b^3 + 9abc + \sqrt{4(-b^2+3ac)^3 + (-27a^2 - 2b^3 + 9abc)^2} \right)^{1/3}}$$
$$+ \frac{\sqrt{3}\left(\begin{array}{l} -27a^2 - 2b^3 + 9abc + \\ \sqrt{4(-b^2+3ac)^3 + (-27a^2 - 2b^3 + 9abc)^2} \end{array} \right)^{1/3}}{6 \times 2^{1/3} a}. \quad (11)$$

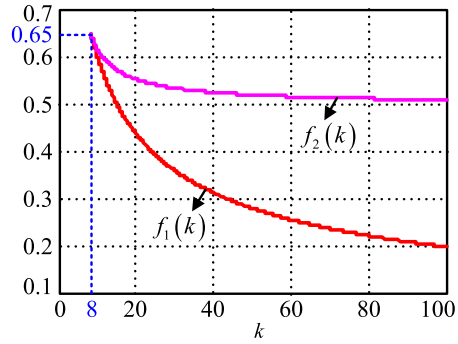

Fig. 4. Curves of $f_1(k)$ and $f_2(k)$.

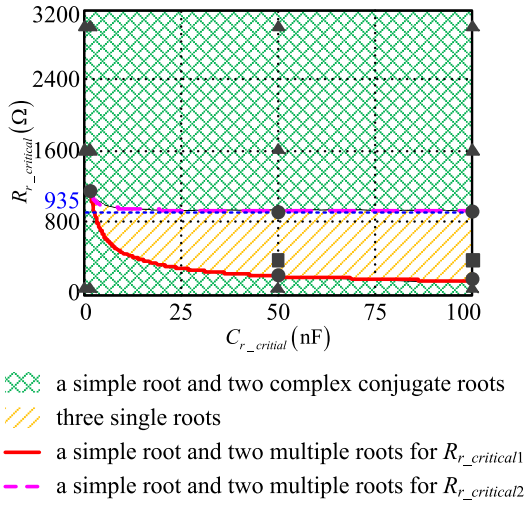

Fig. 5. Distribution of characteristic roots for different *RC* values.

values for $R_{r\_critical1}$ and $R_{r\_critical2}$. Obviously, $k = 8$ yields the maximum value of $R_{r\_critical1}$ and $R_{r\_critical2}$ as

$$R_{r\_critical1\_max} = R_{r\_critical2\_max} = 0.65\sqrt{\frac{L}{C_{eq}}} = 1215\ \Omega. \tag{20}$$

When k tends to infinity, the limit value of $R_{r\_critical1}$ and $R_{r\_critical2}$ are

$$\lim_{k\to\infty} R_{r\_critical1} = 0\ \Omega \tag{21}$$

$$\lim_{k\to\infty} R_{r\_critical2} = 0.5\sqrt{\frac{L}{C_{eq}}} = 935\ \Omega. \tag{22}$$

Therefore, the cutoff points of the three root loci are $R_r = 935\ \Omega$ and $R_r = 1215\ \Omega$, respectively.

According to (18) and (19), the distribution of the characteristic roots for different *RC* values is plotted in Fig. 5. Fig. 6 exhibits the characteristic roots distribution in the root locus diagrams under different *RC* values. As shown in Fig. 6, when C_r changes from zero to infinity, the three characteristic roots move from infinity and "x" symbols to "o" symbols, respectively. There are three cases of root locus depending on the range of R_r, i.e., $R_{r\_small} \le 935\ \Omega$, $935\ \Omega < R_{r\_medium} \le 1215\ \Omega$, and $R_{r\_large} > 1215\ \Omega$. Here, a detailed description of the characteristic roots forms with $R_r = 1$ kΩ and different values of C_r is presented, as shown in the blue solid frame. When $C_r = 1$ nF, the characteristic roots are in the form of " a simple root and two complex conjugate roots" marked by triangles in the root locus diagram. With the *RC* values on the curve of red solid line, the characteristic roots are in the form of "a simple root and two multiple roots," and $C_r = 2.05$ nF can be obtained from $R_r = 1$ kΩ through calculation. In this case, the two conjugate complex roots coincide at the breakaway point near the origin, and in other words, their imaginary part is zero. When $C_r = 3$ nF, the characteristic roots are in the form of "three simple roots." Finally, for the pink doted line, $C_r = 4.8$ nF can be figured out with $R_r = 1$ kΩ, consequently, (6) has two multiple roots at the breakpoint far from the origin and the characteristic roots are in the form of "a simple root and two multiple roots." Considering the length limit, the detailed introduction to the form of characteristic roots with other groups of R_r and C_r values are not given here. In general, when $R_{r\_small} \le 935\ \Omega$ and $935\ \Omega < R_{r\_medium} \le 1215\ \Omega$, three different forms of characteristic roots will appear with different values of C_r. However, for $R_{r\_large} > 1215\ \Omega$, the characteristic roots have only one form of "a simple root and two complex conjugate roots," regardless of the value of C_r.

It should be noted that, in [34], the optimum design of an *RC* snubber to suppress the surge voltage across the transistor in a switching regulator is presented. The surge voltage is analyzed by means of high-frequency equivalent circuits and the third-order characteristic equation about v_{ds} is obtained. Interestingly, (17) in [34] has the same form with (6), whereras the coefficients of the derivative item of each order are different. Therefore, from the viewpoint of control theory, their root locus diagrams are very similar. However, the physical significance of electricity, the objective of research, and the process of utilizing the root locus to analyze problems and achieve goals are different.

According to the derivations of the inductor current, the drain source voltage of the switch and so on in Appendix B, the waveforms of v_{Cr}, i_{RC}, i_L, and v_{ds} for different *RC* values can be drawn. In a half line cycle, depending on whether v_{ds} can oscillate to zero or not, there are two situations about the inductor current. The analysis reveals that the electric interval corresponding to $v_g(n) < V_b$ covers only a minor part of the whole line cycle. In addition, the waveforms of i_L are similar in the two situations. For simplicity, the waveforms at $\pi/4$ where $v_g(n) \ge V_b$ are plotted and presented here.

The waveforms for "a simple root and two complex conjugate roots" are shown in Fig. 7, where the *RC* values represented by the triangles in Fig. 5 are adopted, respectively. It can be seen that i_L oscillates during T_d, where the *RC* values determine the amplitude and frequency of the oscillating current as well as the speed of oscillation attenuation.

For the *RC* values on the curves of red solid line and pink doted line, the characteristic roots are in the form of "a simple root and two multiple roots." Here the *RC* values corresponding to

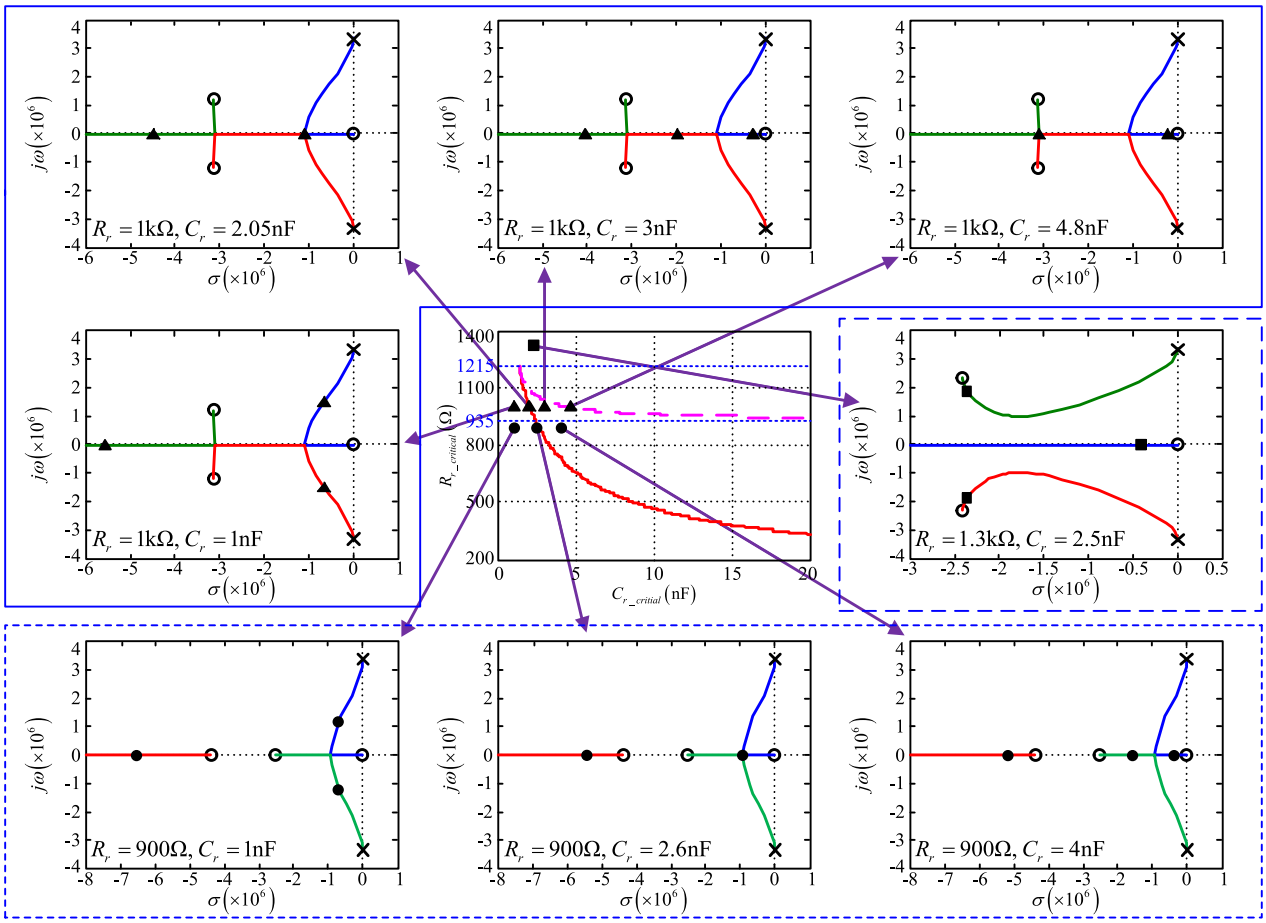

Fig. 6. Root locus diagrams for parameter C_r.

the circles in Fig. 5 are used for drawing Fig. 8. The waveforms indicate that i_L drops first, then it rises and remains stable, and the falling and rising speed lies on the *RC* values.

For the "three simple roots," the waveforms can be considered as the transition between that for red solid line and pink doted line. With the *RC* values marked by squares in Fig. 5, Fig. 9 is plotted.

If the average value in oscillation period and the initial value in a switching cycle are equal to zero, the inductor current will not be disturbed, and the distortion of input current can be eliminated [36]. The average current in the oscillation period and the initial value of the inductor current at the *n*th number of switching cycle can be calculated as, (23) and (24) as shown at the bottom of this page.

Therefore, according to (23) and (24), the waveforms of $i_{L\_\text{initial}}(n)$ and $i_{L\_Td\_\text{ave}}(n)$ in a half line cycle can be plotted in Figs. 10–15.

The aforementioned analysis explicitly shows that whatever the form of the characteristic roots is, for the inductor current, different *RC* values lead to different variation rules of average

$$i_{L\_T_d\_\text{ave}}(n) = \begin{cases} \dfrac{1}{T_s}\int_{(n-1)T_s+T_{\text{on}}+T_{\text{off}}}^{nT_s} i_{L\_T_d}(t)\,dt, v_g(n) \geq V_b \\ \dfrac{1}{T_s}\left[\int_{(n-1)T_s+T_{\text{on}}+T_{\text{off}}}^{nT_s+T_{\text{on}}+T_{\text{off}}+T_{d1}} i_{L\_T_{d1}}(t)\,dt + \int_{nT_s+T_{\text{on}}+T_{\text{off}}+T_{d1}}^{nT_s+T_{\text{on}}+T_{\text{off}}+T_{d1}+T_{d2}} i_{L\_T_{d2}}(t)\,dt \right. \\ \qquad \left. + \int_{nT_s+T_{\text{on}}+T_{\text{off}}+T_{d1}+T_{d2}}^{nT_s} i_{L\_T_{d3}}(t)\,dt\right], v_g(n) < V_b \end{cases} \tag{23}$$

$$i_{L\_\text{initial}}(n) = \begin{cases} i_{L\_T_{d1}}\left((n-2)T_s + T_{\text{on}} + T_{\text{off}} + T_d\right), v_g(n-1) \geq V_b \\ i_{L\_T_{d1}}\left((n-2)T_s + T_{\text{on}} + T_{\text{off}} + T_d\right), v_g(n-1) < V_b \,\&\, T_d \leq T_{d1} \\ i_{L\_T_{d2}}\left((n-2)T_s + T_{\text{on}} + T_{\text{off}} + T_d\right), v_g(n-1) < V_b \,\&\, T_{d1} < T_d \leq T_{d1} + T_{d2} \\ i_{L\_T_{d3}}\left((n-2)T_s + T_{\text{on}} + T_{\text{off}} + T_d\right), v_g(n-1) < V_b \,\&\, T_d > T_{d1} + T_{d2}. \end{cases} \tag{24}$$

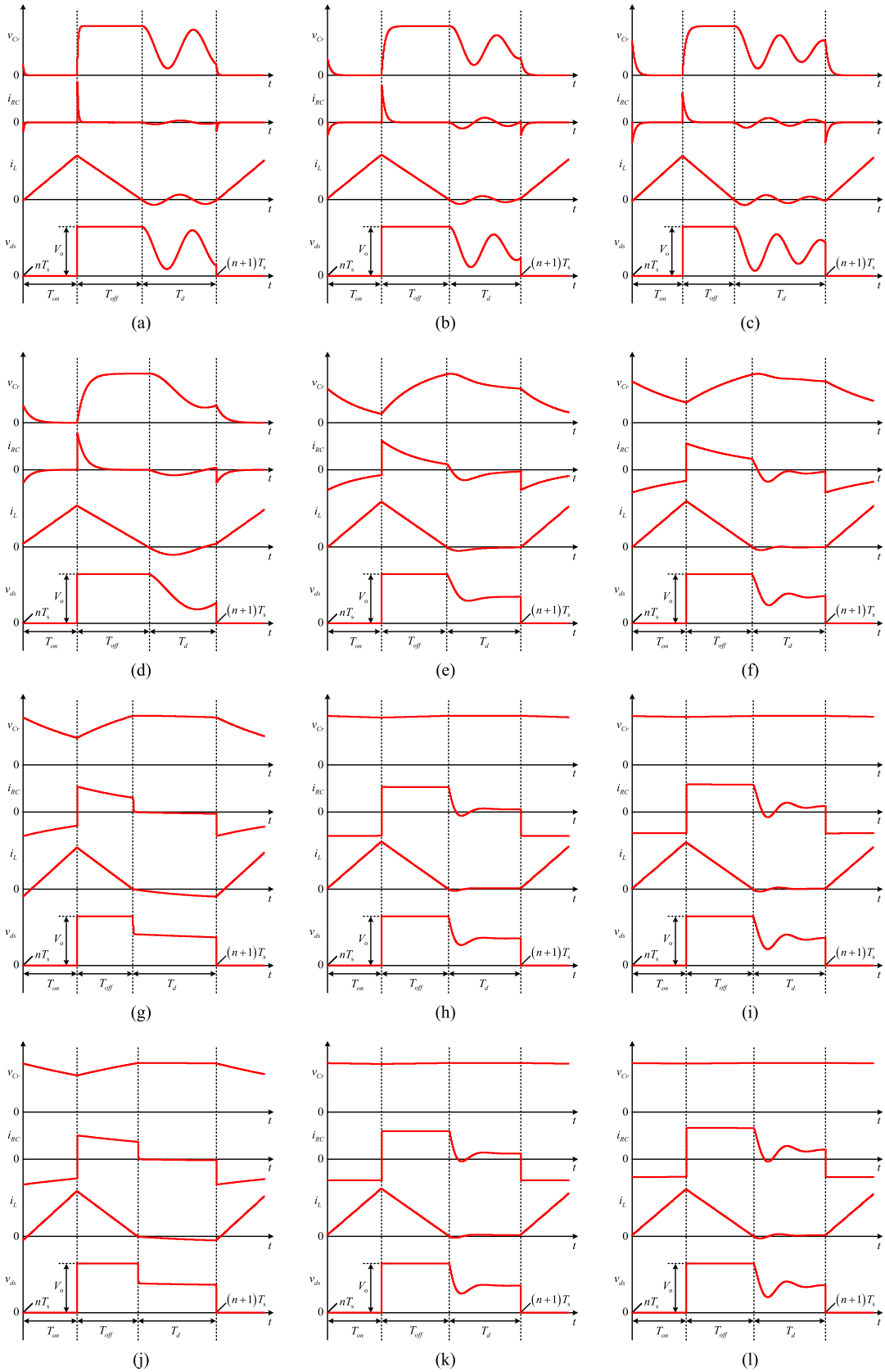

Fig. 7. Waveforms of v_{Cr}, i_{RC}, i_L, and v_{ds} for "a simple root and two complex conjugate roots." (a) $R_r = 100\ \Omega$, $C_r = 100$ pF. (b) $R_r = 1.6$ kΩ, $C_r = 100$ pF. (c) $R_r = 3$ kΩ, $C_r = 100$ pF. (d) $R_r = 100\ \Omega$, $C_r = 1.3$ nF. (e) $R_r = 1.6$ kΩ, $C_r = 1.3$ nF. (f) $R_r = 3$ kΩ, $C_r = 1.3$ nF. (g) $R_r = 100\ \Omega$, $C_r = 50$ nF. (h) $R_r = 1.6$ kΩ, $C_r = 50$ nF. (i) $R_r = 3$ kΩ, $C_r = 50$ nF. (j) $R_r = 100\ \Omega$, $C_r = 100$ nF. (k) $R_r = 1.6$ kΩ, $C_r = 100$ nF. (l) $R_r = 3$ kΩ, $C_r = 100$ nF.

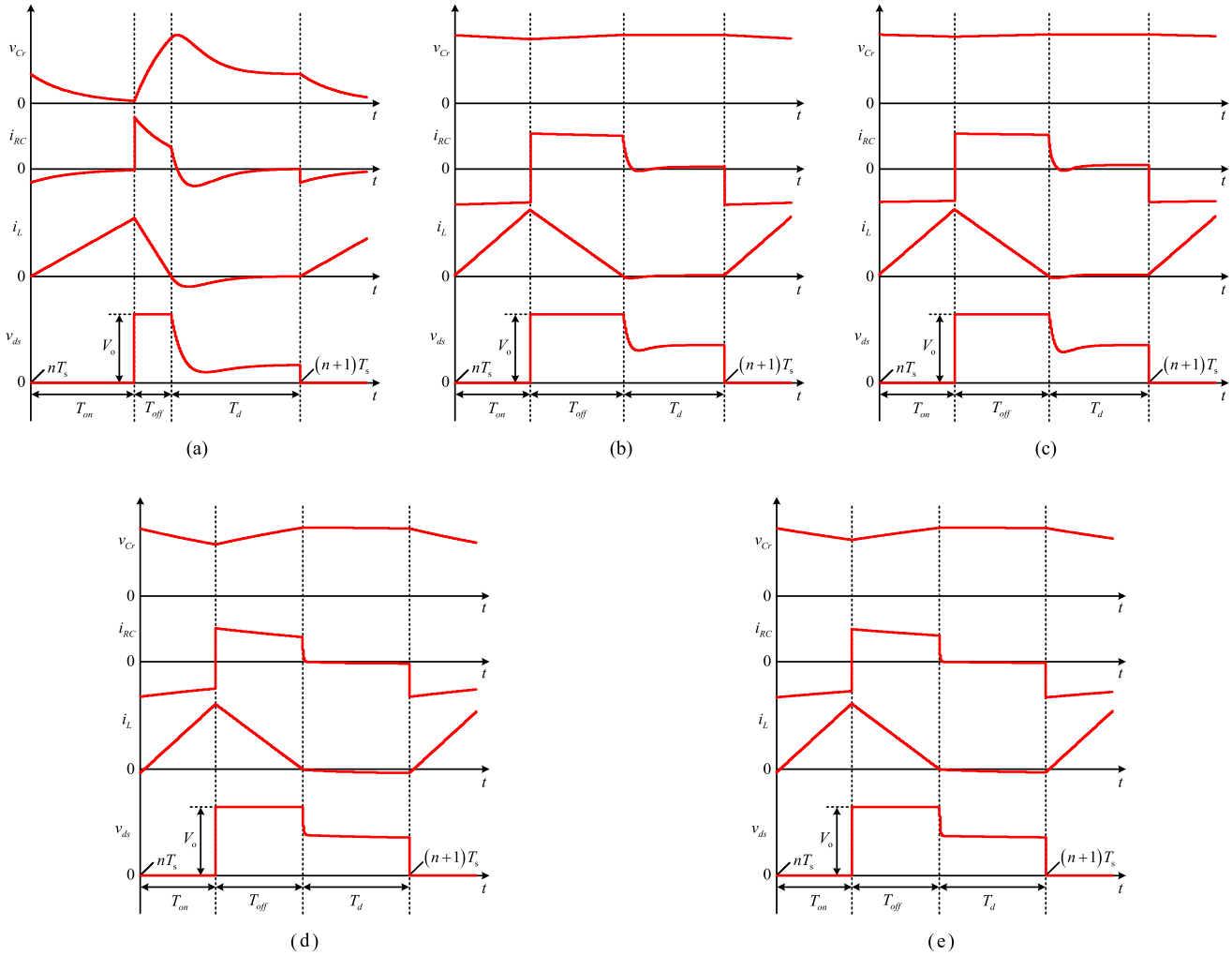

Fig. 8. Waveforms of v_{Cr}, i_{RC}, i_L, and v_{ds} for "a simple root and two multiple roots." (a) $R_r = 1.2$ kΩ, $C_r = 1.3$ nF. (b) $R_r = 941\ \Omega$, $C_r = 50$ nF. (c) $R_r = 938\ \Omega$, $C_r = 100$ nF. (d) $R_r = 211\ \Omega$, $C_r = 50$ nF. (e) $R_r = 149\ \Omega$, $C_r = 100$ nF.

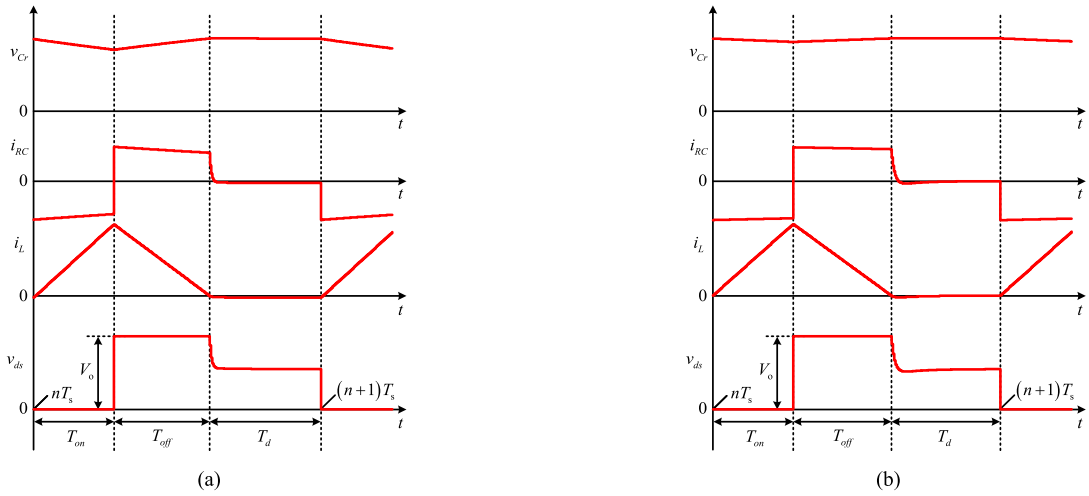

Fig. 9. Waveforms of v_{Cr}, i_{RC}, i_L, and v_{ds} for "three simple roots." (a) $R_r = 350\ \Omega$, $C_r = 50$ nF. (b) $R_r = 350\ \Omega$, $C_r = 100$ nF.

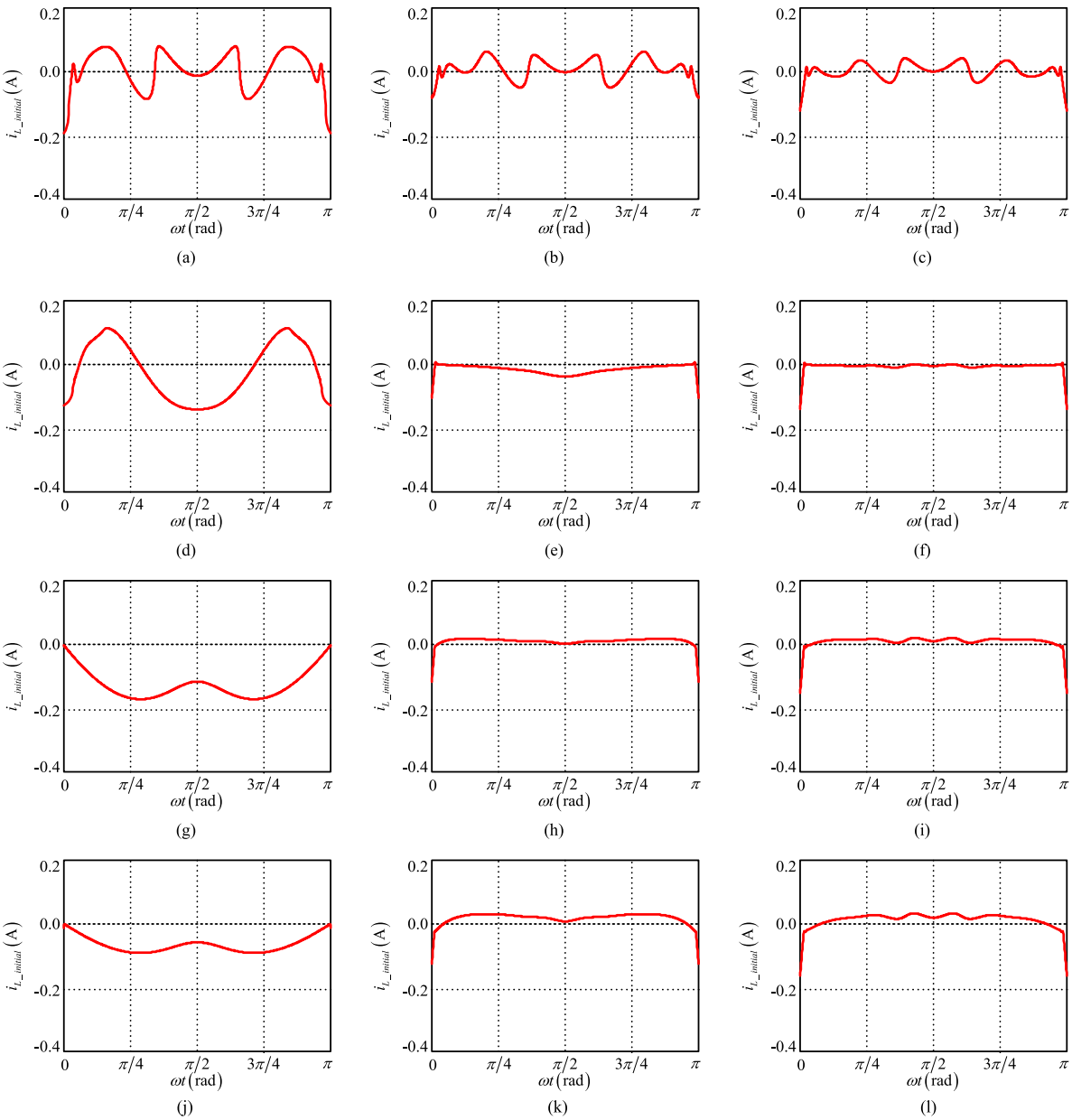

Fig. 10. Waveforms of $i_{L\_\text{initial}}(n)$ for "a simple root and two complex conjugate roots." (a) $R_r = 100\ \Omega$, $C_r = 100$ pF. (b) $R_r = 1.6$ kΩ, $C_r = 100$ pF. (c) $R_r = 3$ kΩ, $C_r = 100$ pF. (d) $R_r = 100\ \Omega$, $C_r = 1.3$ nF. (e) $R_r = 1.6$ kΩ, $C_r = 1.3$ nF. (f) $R_r = 3$ kΩ, $C_r = 1.3$ nF. (g) $R_r = 100\ \Omega$, $C_r = 50$ nF. (h) $R_r = 1.6$ kΩ, $C_r = 50$ nF. (i) $R_r = 3$ kΩ, $C_r = 50$ nF. (j) $R_r = 100\ \Omega$, $C_r = 100$ nF. (k) $R_r = 1.6$ kΩ, $C_r = 100$ nF. (l) $R_r = 3$ kΩ, $C_r = 100$ nF.

value in an oscillation period and initial value in a switching cycle. For a lowest THD, the optimal *RC* values as well as their relationship between the inductance and parasitic capacitance will be calculated in crystal detail in Section III.

III. Parameter Selection of the *RC* Snubber

When the switch turns ON, the inductor current increases linearly

$$i_{L\_T_{\text{on}}}(t) = \frac{v_g(n)}{L}\left[t - (n-1)T_s\right] + i_{L\_\text{initial}}(n) \tag{25}$$

where $(n-1)T_s \le t \le (n-1)T_s + T_{\text{on}}$.

When the switch turns OFF, the inductor current decreases linearly

$$i_{L\_T_{\text{off}}}(t) = i_{L\_T_{\text{on}}}\left((n-1)T_s + T_{\text{on}}\right) - \frac{V_o - v_g(n)}{L}\left[t - (n-1)T_s - T_{\text{on}}\right] \tag{26}$$

where $(n-1)T_s + T_{\text{on}} \le t \le (n-1)T_s + T_{\text{on}} + T_{\text{off}}$, and

$$T_{\text{off}} = \frac{L}{V_o - v_g(n)} i_{L\_T_{\text{on}}}\left((n-1)T_s + T_{\text{on}}\right). \tag{27}$$

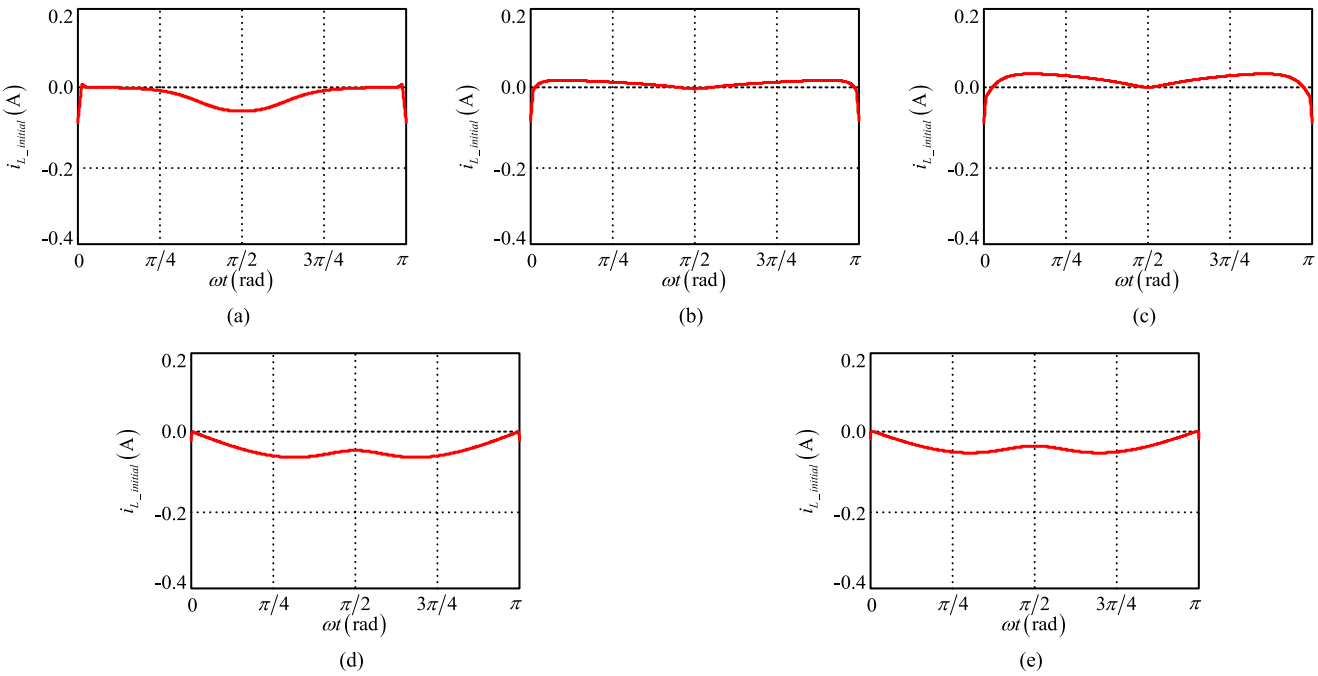

Fig. 11. Waveforms of $i_{L\_initial}(n)$ for "a simple root and two multiple roots." (a) $R_r = 1.2$ kΩ, $C_r = 1.3$ nF. (b) $R_r = 941$ Ω, $C_r = 50$ nF. (c) $R_r = 938$ Ω, $C_r = 100$ nF. (d) $R_r = 211$ Ω, $C_r = 50$ nF. (e) $R_r = 149$ Ω, $C_r = 100$ nF.

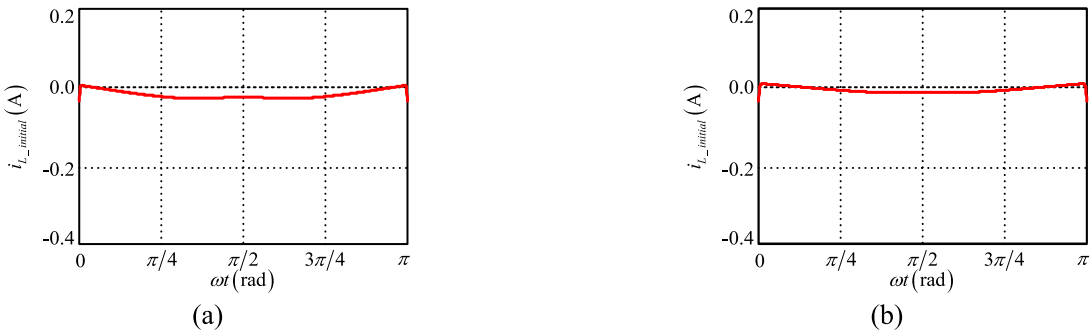

Fig. 12. Waveforms of $i_{L\_initial}(n)$ for "three simple roots." (a) $R_r = 350$ Ω, $C_r = 50$ nF. (b) $R_r = 350$ Ω, $C_r = 100$ nF.

Therefore, the average current in a switching cycle can be formulated as

$$i_{\text{in}}(n) = \begin{cases} \dfrac{1}{T_s}\left[\begin{array}{l} \int_{(n-1)T_s}^{(n-1)T_s+T_{\text{on}}} i_{L\_T_{\text{on}}}(t)\,dt \\ +\int_{(n-1)T_s+T_{\text{on}}}^{(n-1)T_s+T_{\text{on}}+T_{\text{off}}} i_{L\_T_{\text{off}}}(t)\,dt \\ +\int_{(n-1)T_s+T_{\text{on}}+T_{\text{off}}}^{nT_s} i_{L\_T_d}(t)\,dt \end{array}\right], v_g(n) \geq V_b \\ \dfrac{1}{T_s}\left[\begin{array}{l} \int_{(n-1)T_s}^{(n-1)T_s+T_{\text{on}}} i_{L\_T_{\text{on}}}(t)\,dt \\ +\int_{(n-1)T_s+T_{\text{on}}}^{(n-1)T_s+T_{\text{on}}+T_{\text{off}}} i_{L\_T_{\text{off}}}(t)\,dt \\ +\int_{(n-1)T_s+T_{\text{on}}+T_{\text{off}}}^{nT_s+T_{\text{on}}+T_{\text{off}}+T_{d1}} i_{L\_T_{d1}}(t)\,dt \\ +\int_{nT_s+T_{\text{on}}+T_{\text{off}}+T_{d1}}^{nT_s+T_{\text{on}}+T_{\text{off}}+T_{d1}+T_{d2}} i_{L\_T_{d2}}(t)\,dt \\ +\int_{nT_s+T_{\text{on}}+T_{\text{off}}+T_{d1}+T_{d2}}^{nT_s} i_{L\_T_{d3}}(t)\,dt \end{array}\right], v_g(n) < V_b \end{cases} \tag{28}$$

The THD of the input current is expressed as

$$\text{THD} = \sqrt{\frac{I_{\text{in\_rms}}^2 - I_1^2}{I_1^2}} \times 100\% \tag{29}$$

where $I_{\text{in\_rms}}$ is the root mean square (rms) value of the input current, I_1 is the rms value of the fundamental component of the input current, which are formulated as

$$I_{\text{in\_rms}} = \sqrt{\frac{1}{T_l}\sum_{n=0}^{T_l/T_s} i_{\text{in}}^2(n)\,T_s} \tag{30}$$

$$I_1 = \frac{\sqrt{2}}{T_l}\sum_{n=0}^{T_l/T_s} i_{\text{in}}(n)\,T_s \sin\frac{2\pi n T_s}{T_l} \tag{31}$$

where T_l is the line cycle.

Substituting the formulas (A5)–(A27) in Appendix B into (29)–(31), the THD can be obtained.

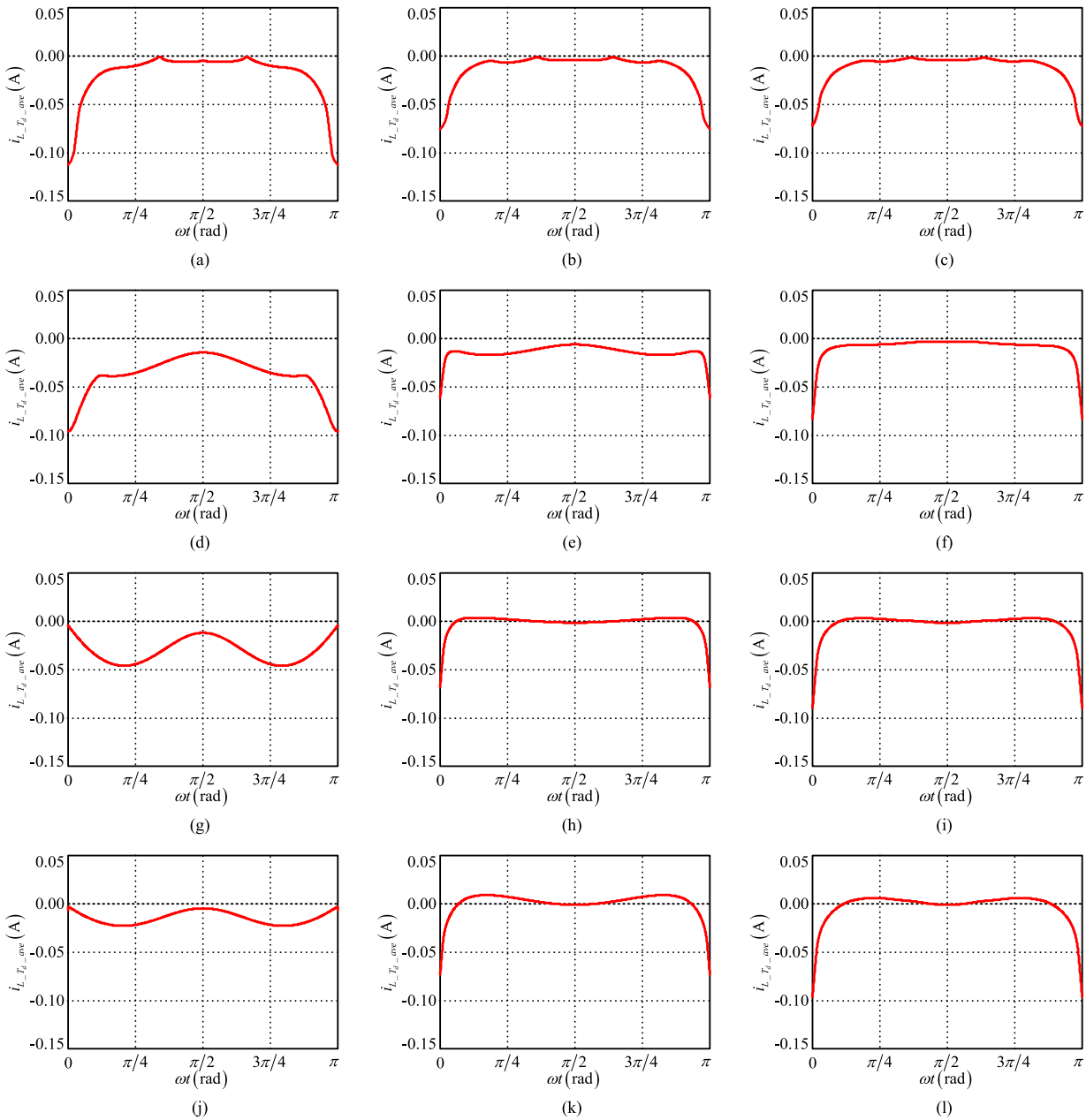

Fig. 13. Waveforms of $i_{L\_Td\_ave}(n)$ for "a simple root and two complex conjugate roots." (a) $R_r = 100\ \Omega$, $C_r = 100$ pF. (b) $R_r = 1.6$ kΩ, $C_r = 100$ pF. (c) $R_r = 3$ kΩ, $C_r = 100$ pF. (d) $R_r = 100\ \Omega$, $C_r = 1.3$ nF. (e) $R_r = 1.6$ kΩ, $C_r = 1.3$ nF. (f) $R_r = 3$ kΩ, $C_r = 1.3$ nF. (g) $R_r = 100\ \Omega$, $C_r = 50$ nF. (h) $R_r = 1.6$ kΩ, $C_r = 50$ nF. (i) $R_r = 3$ kΩ, $C_r = 50$ nF. (j) $R_r = 100\ \Omega$, $C_r = 100$ nF. (k) $R_r = 1.6$ kΩ, $C_r = 100$ nF. (l) $R_r = 3$ kΩ, $C_r = 100$ nF.

IEC 61000-3-2 standards specify that the harmonic limit should be considered for the input power more than 75 W. Referring to the circuit parameters in Section IV, $V_{\text{in\_rms}}$ and P_o are chosen as 220 V_{AC} and 88 W, respectively, for the analysis of the THD of input current.

Based on (29)–(31) and Fig. 5, for a given value of C_r, the curve diagrams about THD versus R_r are depicted in Fig. 16. Fig. 16 reveals that, when C_r is constant, with the increase of R_r, THD decreases first and then increases, hence there is a minimum value of $\text{THD}_{\min\_Cr}$, resulting from a corresponding optimal $R_{r\_\text{optimal}\_Cr}$ with different values of C_r, for which the curves are plotted in the solid line in Fig. 17.

It should be noted that the discrete points in the solid curve about $R_{r\_\text{optimal}\_Cr}$ versus C_r are the one by one calculation results by the software Mathcad. In order to show the relationship clearly, the following fitting function of explicit expression is figured out, which is drawn in the dotted line in Fig. 17

$$R_{r\_\text{optimal}\_Cr\_fit} = \sqrt{\frac{L\left(2.411C_r + 5.505C_{\text{eq}}\right)}{C_{\text{eq}}\left(C_r + 0.518C_{\text{eq}}\right)}}. \tag{32}$$

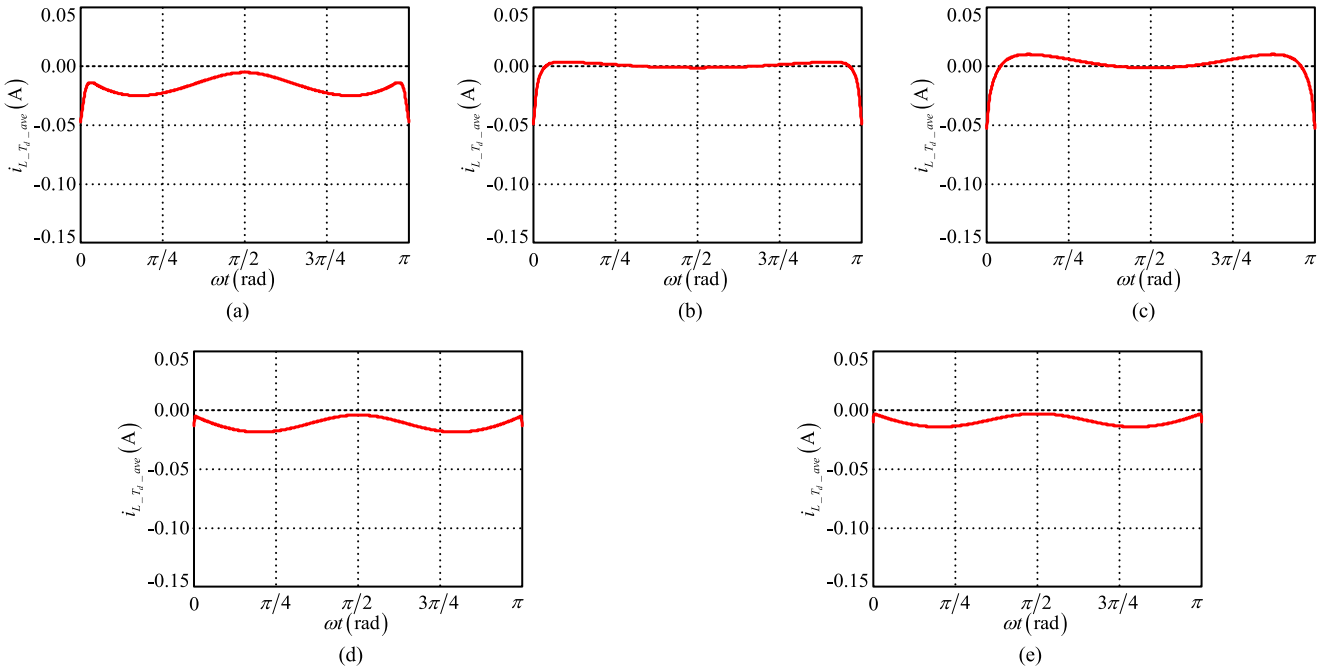

Fig. 14. Waveforms of $i_{L\_Td\_ave}(n)$ for "a simple root and two multiple roots." (a) $R_r = 1.2$ kΩ, $C_r = 1.3$ nF. (b) $R_r = 941\ \Omega$, $C_r = 50$ nF. (c) $R_r = 938\ \Omega$, $C_r = 100$ nF. (d) $R_r = 211\ \Omega$, $C_r = 50$ nF. (e) $R_r = 149\ \Omega$, $C_r = 100$ nF.

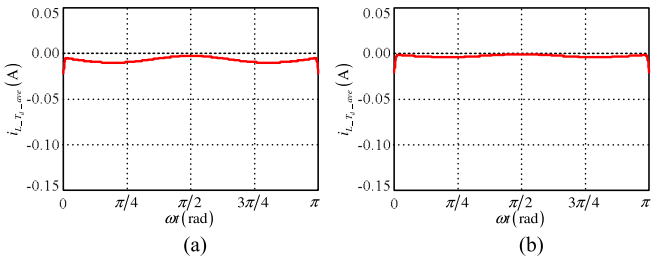

Fig. 15. Waveforms of $i_{L\_Td\_ave}(n)$ for "three simple roots." (a) $R_r = 350\ \Omega$, $C_r = 50$ nF. (b) $R_r = 350\ \Omega$, $C_r = 100$ nF.

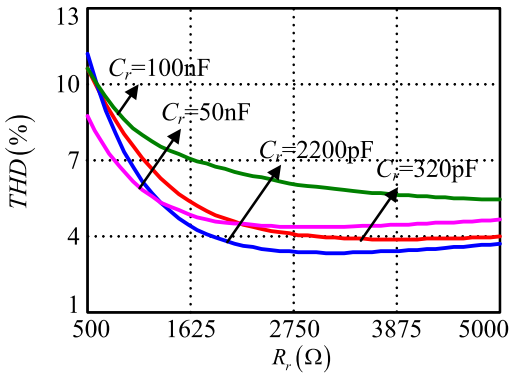

Fig. 16. Relationship between THD and R_r while C_r is constant.

Based on (29)–(32), the relationship between $\mathrm{THD}_{\min\_Cr}$ and C_r is depicted in Fig. 18. Fig. 18 shows that, with the increase of C_r, $\mathrm{THD}_{\min\_Cr}$ decreases first and then increases,

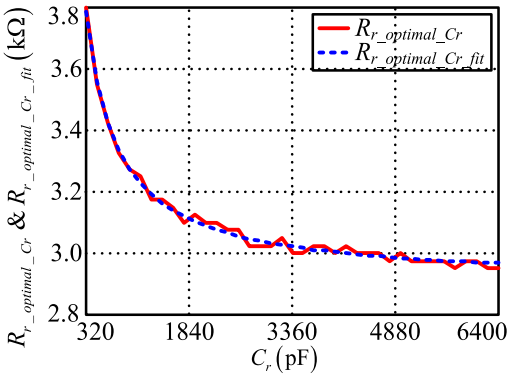

Fig. 17. Relationship between $R_{r\_optimal\_Cr}$ and C_r.

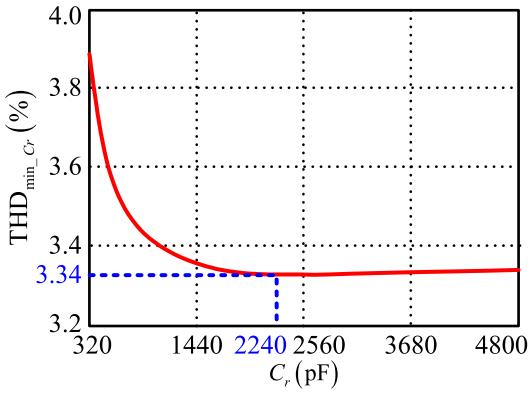

Fig. 18. Relationship between $\mathrm{THD}_{\min\_Cr}$ and C_r.

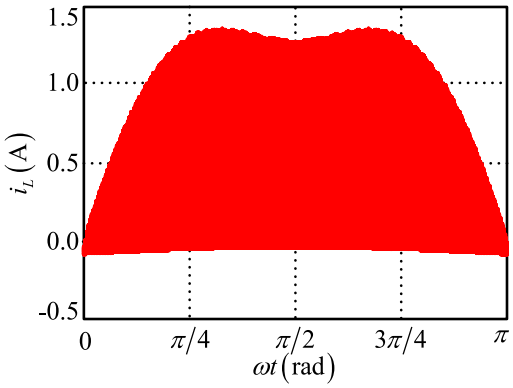

Fig. 19. Theoretical waveform of inductor current with optimal *RC* values.

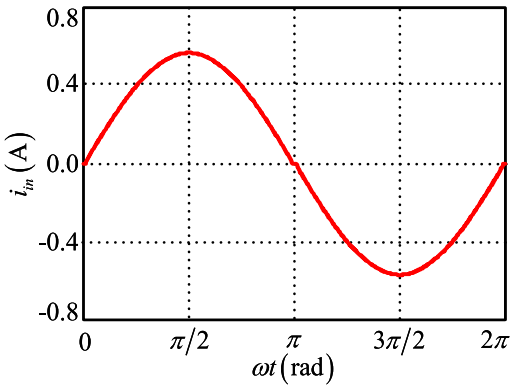

Fig. 20. Theoretical waveforms of input current with optimal *RC* values.

and the minimum value is 3.34%, which is corresponding to $R_{r\_\text{optimal}} = 3068\ \Omega$ and $C_{r\_\text{optimal}} = 2280$ pF. Considering the analysis in Section II, we can notice that the optimal *RC* values are in the group of "a simple root and two complex conjugate roots." Among all the drawings in Figs. 7, 10, and 13, Figs. 7(f), 10(f), and 13(f) are most close to that of the optimal values. Considering the parameter of the converter, the relationship between this value and the inductance as well as parasitic capacitance is obtained as

$$R_{r\_\text{optimal}} = 1.64\sqrt{\frac{L}{C_{\text{eq}}}} \tag{33}$$

$$C_{r\_\text{optimal}} = 14.25C_{\text{eq}}. \tag{34}$$

From (25)–(28), the waveforms of i_L and i_{in} with optimal *RC* values in a half line cycle can be drawn in Figs. 19 and 20.

In [36], the oscillation process of a boost PFC converter operated in DCM without *RC* snubber is analyzed in detail. Based on the mathematical expressions presented in [36], the waveforms of $i_{L\_\text{initial}}(n)$, $i_{L\_Td\_\text{ave}}(n)$, i_L, and i_{in} in a half line cycle are presented in Figs. 21–24, respectively. Compared with that in Fig. 24, the theoretical input current in Fig. 20 with optimal *RC* values is greatly improved and nearly sinusoidal.

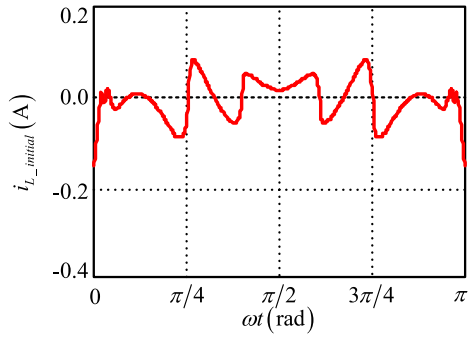

Fig. 21. Waveform of initial value of inductor current without *RC*.

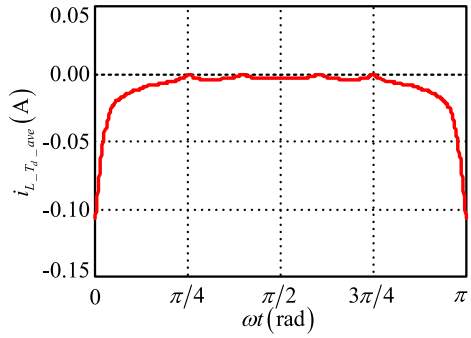

Fig. 22. Waveform of average value of inductor current in oscillation period without *RC*.

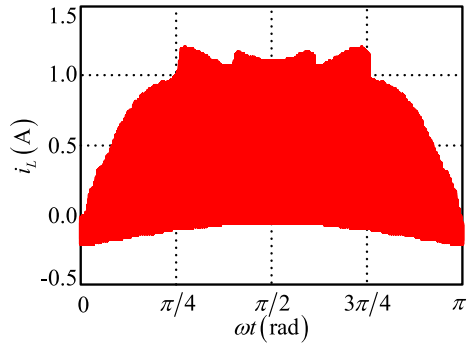

Fig. 23. Theoretical waveform of inductor current without *RC*.

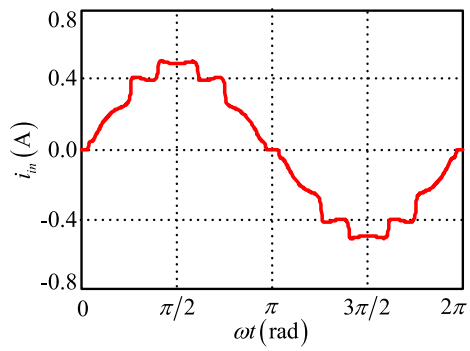

Fig. 24. Theoretical waveforms of input current without *RC*.

TABLE I
OPTIMAL *RC* VALUES FOR DIFFERENT RATED LOAD WITH THE SWITCHING DEVICES SELECTED FROM INFINEON

Rated load	L	Power switch	Power diode	C_{eq}	Z_n	$R_{r\_optimal}/Z_n$	$C_{r\_optimal}/Z_n$
500W	1120μH	IPP60R250CP C_{oss}=54pF	IDH03SG60C C_D=8pF	62pF	4250Ω	1.68	14.4
1500W	374μH	IPP60R099C6 C_{oss}=154pF	IDH06SG60C C_D=20pF	174pF	1466Ω	1.66	14.1
2500W	224μH	IPP60R074C6 C_{oss}=170pF	IDH10SG60C C_D=40pF	210pF	1033Ω	1.73	15.2
3500W	160μH	IPW65R019C7 C_{oss}=160pF	IDH16G65C6 C_D=46pF	206pF	881Ω	1.78	15.9

TABLE II
OPTIMAL *RC* VALUES FOR DIFFERENT RATED LOAD WITH THE SWITCHING DEVICES SELECTED FROM FAIRCHILD

Rated load	L	Power switch	Power diode	C_{eq}	Z_n	$R_{r\_optimal}/Z_n$	$C_{r\_optimal}/Z_n$
500W	1120μH	FCP260N60E C_{oss}=32pF	FFSP0665A C_D=32pF	64pF	4183Ω	1.70	14.4
1500W	374μH	FCH104N60N C_{oss}=75pF	FFSP0865A C_D=38pF	113pF	1819Ω	1.77	15.2
2500W	224μH	FCH072N60F C_{oss}=110pF	FFSP1065A C_D=47pF	157pF	1194Ω	1.76	15.5
3500W	160μH	FCH041N60E C_{oss}=187pF	FFSP1665A C_D=72pF	259pF	786Ω	1.74	15.3

TABLE III
OPTIMAL *RC* VALUES FOR DIFFERENT RATED LOAD WITH THE SWITCHING DEVICES SELECTED FROM ST

Rated load	L	Power switch	Power diode	C_{eq}	Z_n	$R_{r\_optimal}/Z_n$	$C_{r\_optimal}/Z_n$
500W	1120μH	STW18N65M5 C_{oss}=32pF	STPSC6H065 C_D=30pF	62pF	4250Ω	1.68	14.4
1500W	374μH	STW45N65M5 C_{oss}=82pF	STPSC8H065 C_D=38pF	120pF	1765Ω	1.76	15.1
2500W	224μH	STW69N65M5 C_{oss}=170pF	STPSC10H065 C_D=48pF	218pF	1014Ω	1.72	15.4
3500W	160μH	STW88N65M5 C_{oss}=223pF	STPSC16H065C C_D=38pF	261pF	783Ω	1.74	15.2

TABLE IV
OPTIMAL *RC* VALUES FOR DIFFERENT RATED LOAD WITH THE SWITCHING DEVICES SELECTED FROM TOSHIBA

Rated load	L	Power switch	Power diode	C_{eq}	Z_n	$R_{r\_optimal}/Z_n$	$C_{r\_optimal}/Z_n$
500W	1120μH	TK10E60W C_{oss}=20pF	TRS6A65C C_D=35pF	55pF	4513Ω	1.74	14.9
1500W	374μH	TK31E60W C_{oss}=70pF	TRS8A65C C_D=44pF	114pF	1811Ω	1.78	15.2
2500W	224μH	TK39N60X C_{oss}=90pF	TRS10A65C C_D=55pF	145pF	1243Ω	1.79	15.7
3500W	160μH	TK62N60X C_{oss}=140pF	TRS16A65C C_D=88pF	228pF	838Ω	1.76	15.5

It should be noted that for other boost PFC converters, the same method can be used for the analysis and calculation, and then the corresponding optimal *RC* parameter can be searched and selected. CCM boost PFC converters are usually designed in the range of hundreds of watts to several kilowatts, the converter parameters and optimal *RC* values can be calculated, as shown in Tables I–IV, where Z_n equals to $\sqrt{L/C_{\rm eq}}$.

IV. EXPERIMENTAL VERIFICATION

For the validity of the proposed method, a 1-kW boost PFC converter based on DSP MC56F8257 has been built and tested in DCM operation. The variable duty cycle strategy proposed in [15] is adopted. The theoretical critical load power of the converter is 96 W at 220 $\rm V_{AC}$. In the following experiments, 88 W is employed as the margin is considered. The specifications and components of the prototype are as follows: $V_{\rm in\_rms}$ = 176–264 V, $f_{\rm l}$ = 50 Hz, $f_{\rm s}$ = 100 kHz, $P_{\rm o}$ = 24 ∼ 88 W, $V_{\rm o}$ = 400 V, L = 560 μH, $C_{\rm oss}$ = 130 pF, $C_{\rm D}$ = 30 pF, $C_{\rm DL}$ = 30 pF, $C_{\rm in}$ = 0.33 μF, and $C_{\rm o}$ = 1000 μF. Power switch: IPP60R099CP, power diode: IDH05S60C, series diode: RURP8120. *RC* snubber: $R_r = 3\,\rm k\Omega$, $C_r = 2.2$ nF (selection principle in this paper); $R_r = 2\,\rm k\Omega$, $C_r = 470$ pF (selection principle in [35]).

The waveforms of the input voltage, input current, and inductor current are presented in Figs. 25 and 26 without

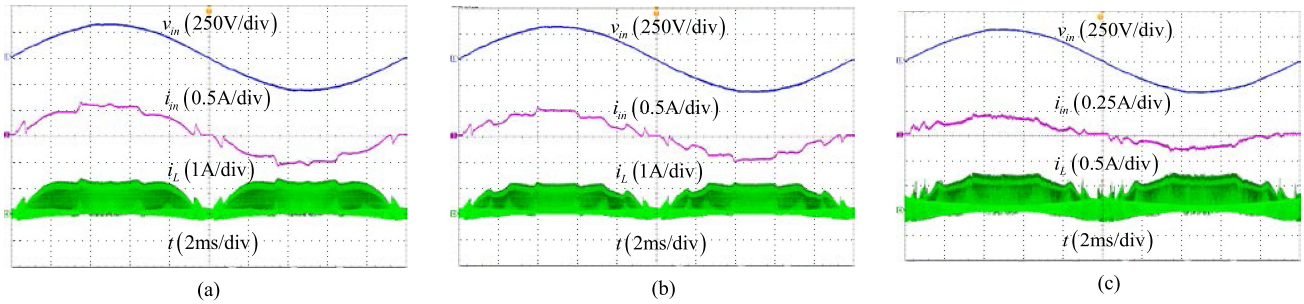

Fig. 25. Experimental waveforms without *RC* at 220 V_{AC}. (a) Po = 88 W. (b) Po = 60 W. (c) Po = 24 W.

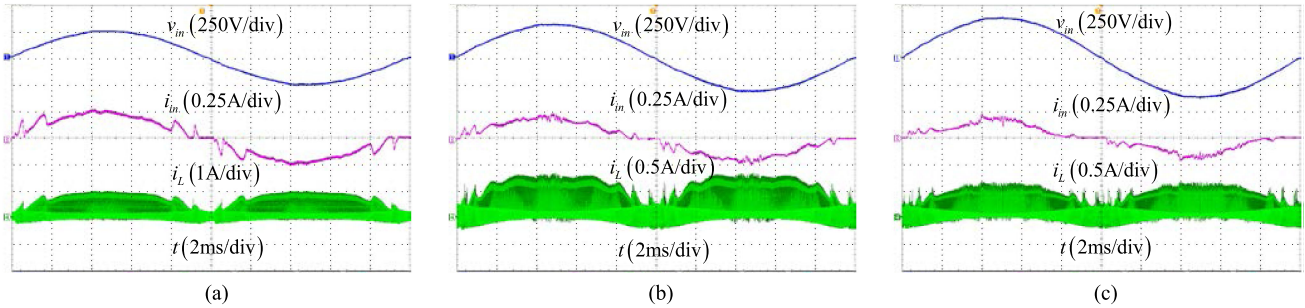

Fig. 26. Experimental waveforms without *RC* while Po = 30 W. (a) 176 V. (b) 220 V. (c) 264 V.

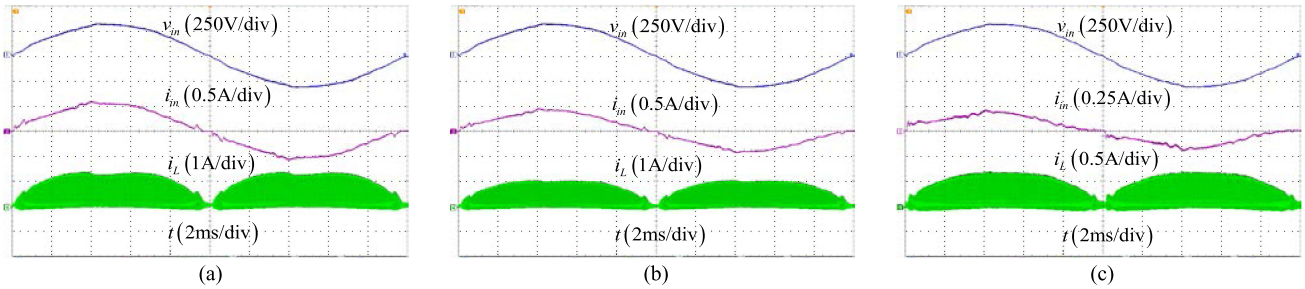

Fig. 27. Experimental waveforms with $R_r = 3\ \text{k}\Omega$, $C_r = 2.2$ nF at 220 V_{AC}. (a) $P_o = 88$ W. (b) $P_o = 60$ W. (c) $P_o = 24$ W.

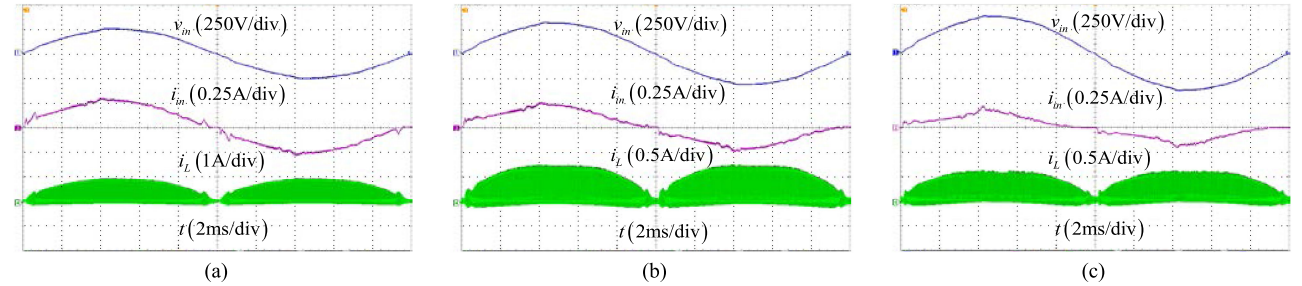

Fig. 28. Experimental waveforms with $R_r = 3\ \text{k}\Omega$, $C_r = 2.2$ nF, while $P_o = 30$ W. (a) 176 V. (b) 220 V. (c) 264 V.

any oscillation suppression circuit, and Figs. 27 and 28 with $R_r = 3\ \text{k}\Omega$, $C_r = 2.2$ nF, respectively. Figs. 25 and 26 show that when a CCM boost PFC converter operates in DCM, the input current is distorted seriously. It can be seen from Figs. 27 and 28 that the input current is improved effectively, especially when at a high power or at a low input voltage.

The waveforms of v_{Cr}, i_{RC}, i_L, and v_{ds} in a switching cycle with $R_r = 3\ \text{k}\Omega$, $C_r = 2.2$ nF are shown in Fig. 29 while $V_{\text{in\_rms}} = 220$ V and $P_o = 60$ W. Fig. 29 illustrates that the waveforms of v_{Cr}, i_{RC}, i_L, and v_{ds} are the same as those of the theoretical analysis, and the inductor current is almost zero at the initial instant of the switching cycle.

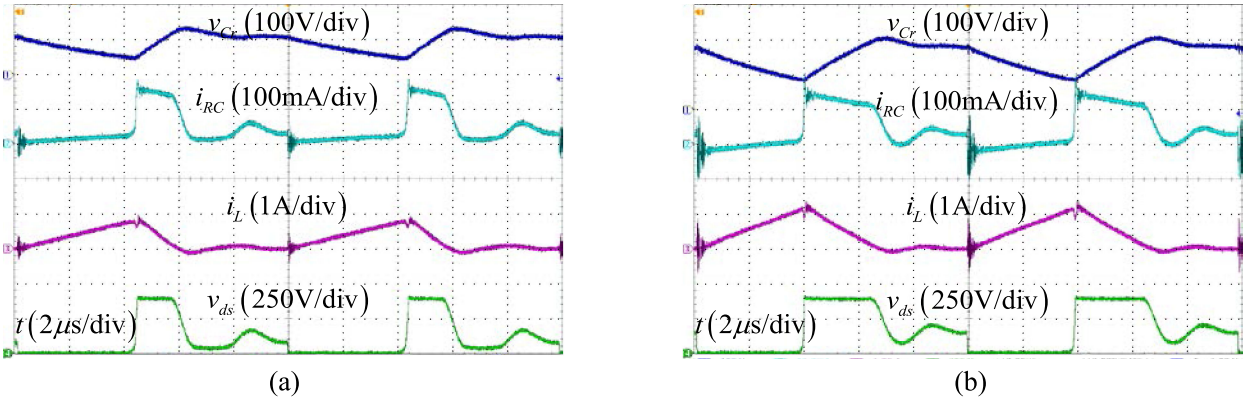

Fig. 29. Waveforms of v_{Cr}, i_{RC}, i_L, and v_{ds} with $R_r = 3$ kΩ, $C_r = 2.2$ nF. (a) $v_g(n) < V_b$. (b) $v_g(n) \geq V_b$.

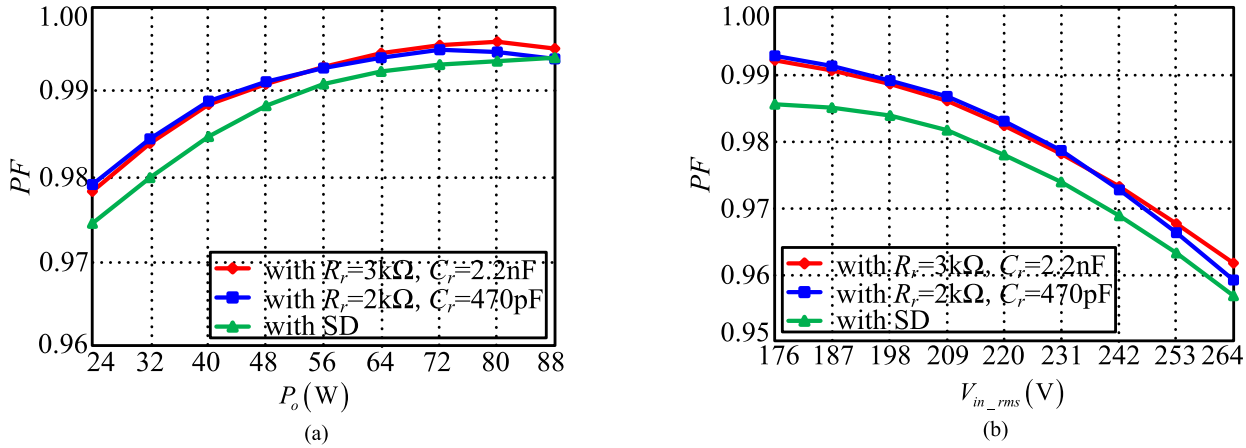

Fig. 30. Measured PF. (a) With different P_{o} at 220 $\mathrm{V_{AC}}$. (b) With different $V_{\mathrm{in\_rms}}$ while $P_{\mathrm{o}} = 30$ W.

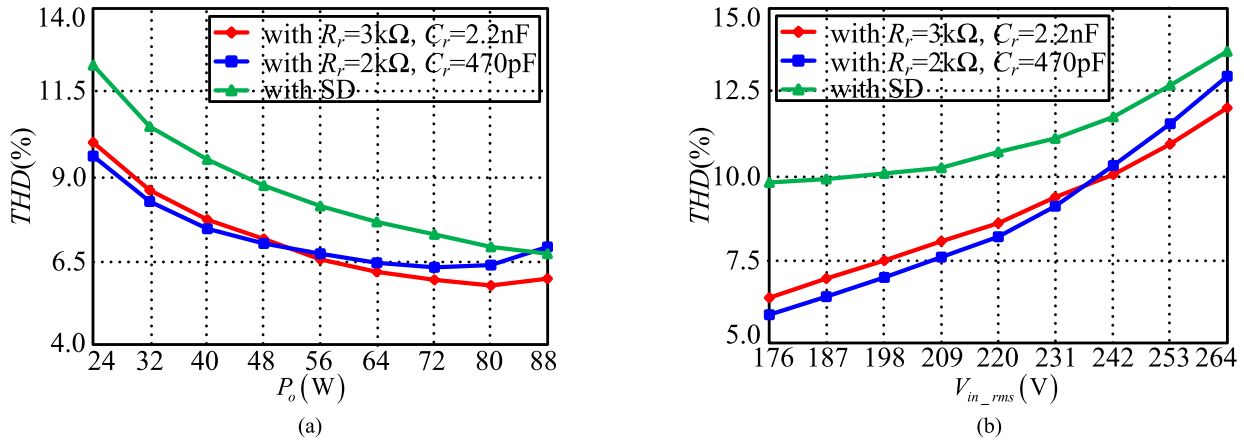

Fig. 31. Measured THD. (a) With different P_{o} at 220 $\mathrm{V_{AC}}$. (b) With different $V_{\mathrm{in\_rms}}$ while $P_{\mathrm{o}} = 30$ W.

The PF and THD curves from experimental results of the converter with $R_r = 3$ kΩ, $C_r = 2.2$ nF, with $R_r = 2$ kΩ, $C_r = 470$ pF, and with series diode (SD) method proposed in [36] at different load power and input voltages are given in Figs. 30 and 31, respectively. The results demonstrate that *RC* snubber can effectively decrease the input current distortion and improve the power factor, and the PF is higher than that with SD. The PF and THD of the converter with two different *RC* values are basically the same. At a certain input voltage, the THD decreases with the increment of the output power, while at a certain output power,

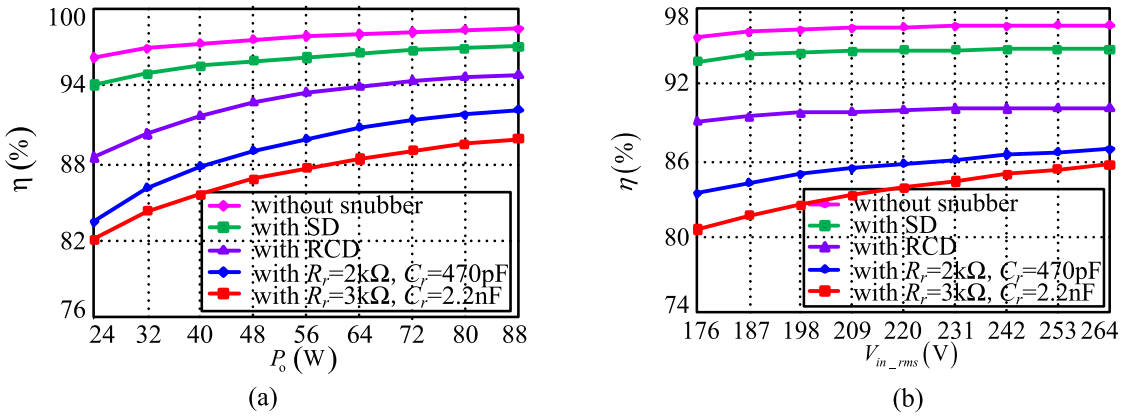

Fig. 32. Measured efficiency. (a) Efficiency curves with different $P_{\rm o}$ at 220 $\rm V_{AC}$. (b) Efficiency curves with different $V_{\rm in\_rms}$ while $P_{\rm o} = 30$ W.

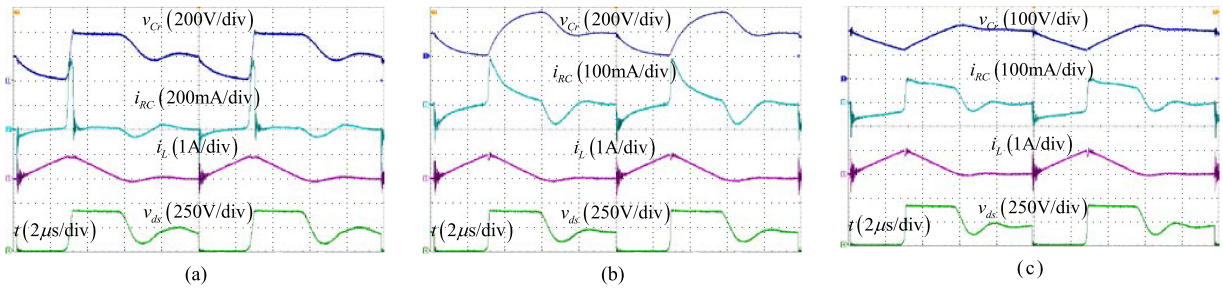

Fig. 33. Waveforms of $v_{\rm Cr}$, $i_{\rm RC}$, i_L, and $v_{\rm ds}$ at $\pi/4$ of a half line cycle. (a) With *RCD*. (b) With $R_r = 2$ kΩ, $C_r = 470$ pF. (c) With $R_r = 3$ kΩ, $C_r = 2.2$ nF.

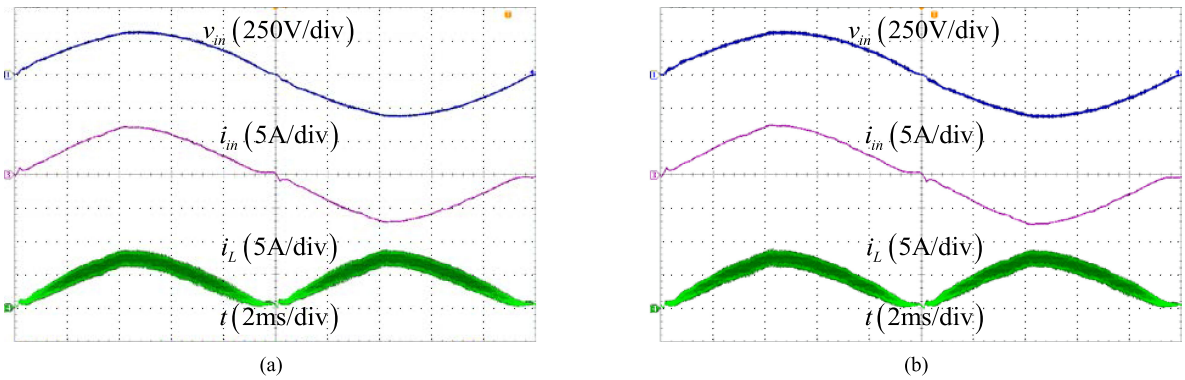

Fig. 34. Experimental waveforms while $V_{\rm in\_rms} = 220$ V and $P_{\rm o} = 1$ kW. (a) Without *RC*. (b) With *RC*.

the THD increases with the increment of the input voltage, both for the converter with *RC* and with SD. The contrary is the case for PF.

Fig. 32 demonstrates the efficiency curves, where the efficiency of the converter with RCD is higher than that with RC. The reasons are explained as follows. The waveforms of $v_{\rm Cr}$, $i_{\rm RC}$, i_L, and $v_{\rm ds}$ at $\pi/4$ of a half line cycle with *RC* and *RCD* are shown in Fig. 33. It is clear to see that, when the switch turns OFF, an inrush current passes the diode of *RCD* and $v_{\rm Cr}$ increases to V_o immediately, then $i_{\rm RC}$ remains at zero till i_L drops to zero. Therefore, the loss of *RCD* is lower than that of *RC*. In addition, it can be seen from Fig. 33(b) and (c) that the rms values of $i_{\rm RC}$ in a switching cycle are nearly the same, whereas R_r is 2 and 3 kΩ, respectively. The loss is different accordingly. Therefore, the *RC* values have a significant effect on the efficiency. However, it can be seen from Fig. 16 that when 320 pF $< C_r <$ 2.2 nF and $R_r >$ 1.6 kΩ, *RC* values have little influence on THD, with which the results in Fig. 31 are in accordance. Actually, this provides a proper range from which the *RC* values can be adjusted and selected according to the performance requirements of the converter in real applications.

For the boost PFC converter, it operates in CCM mode under heavy load, and the THD in this condition will be more important than that under light load. For $V_{\rm in\_rms} = 220$ V and $P_{\rm o} = 1$ kW, the waveforms of $v_{\rm in}$, $i_{\rm in}$, and i_L in a line cycle and in switching cycles at $\pi/4$ of a half line cycle are presented in

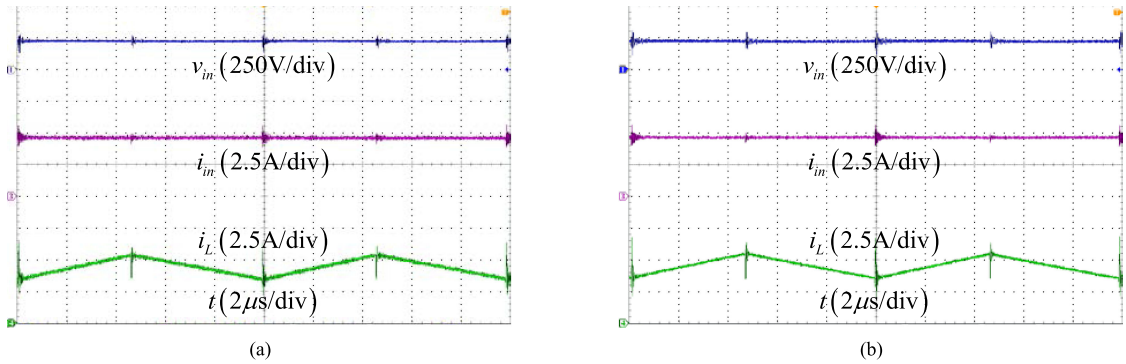

Fig. 35. Experimental waveforms in switching cycles at $\pi/4$ of a half line cycle. (a) Without *RC*. (b) With *RC*.

Figs. 34 and 35, respectively, from which it can be clearly noticed that the waveforms are very similar. Actually, under this condition, the measured PF of the converter without and with *RC* are both 0.994. In consequence, *RC* snubber has a very little influence on the THD of the converter operating in CCM under heavy load.

It should be noted that, when the converter operates in DCM with low power, the *RC* snubber brings about a lower THD and a lower efficiency, compared with SD. When the converter operates in CCM with high power, the efficiency reduction is nearly the same and the influence on THD is nearly zero for the two methods. However, the cost of SD is higher than that of *RC*, for the voltage rating of the diode is higher than 1000 V. Furthermore, for the converter designed in CCM, the DCM covers only a little portion and the CCM takes the most part of the whole operation time. Therefore, from our view point, the solution of *RC* snubber is better than that of SD.

V. Conclusion

The influence of *RC* snubber on the oscillation process of DCM boost PFC converter is analyzed, and the related mathematical expressions are derived and presented in detail for different kinds of *RC* values. The THD of the input current is figured out at different *RC* parameters, and the optimal *RC* values as well as their relationship between the inductance and parasitic capacitance is discovered. The analysis shows that, with the optimal *RC* snubber, the initial value of the inductor current in a switching cycle and the average value of the inductor current in an oscillation period is approximately zero. In consequence, the distortion of input current can be greatly reduced.

Appendix

A. Derivation of (18) and (19)

Defining $C_{r\_\text{critical}} = kC_{\text{eq}}$ and substituting it into (17) leads to

$$(k+1)\,C_{\text{eq}}^2 L^2\gamma^4 + (2-k)\,C_{\text{eq}}L\gamma^2 + 1 = 0. \tag{A1}$$

From (A1), the following equation can be obtained:

$$\gamma^2 = \frac{(k-2) \pm \sqrt{k\,(k-8)}}{2\,(k+1)\,C_{\text{eq}}L}. \tag{A2}$$

Substitution of (A2) into (16) results in

$$R_{r\_\text{critical}} = \frac{2L\sqrt{\frac{(k-2)\pm\sqrt{k(k-8)}}{2(k+1)C_{\text{eq}}L}}}{\left(\frac{(k-2)\pm\sqrt{k(k-8)}}{2(k+1)}+1\right)^2}. \tag{A3}$$

(A3) can be rearranged as

$$R_{r\_\text{critical}} = \frac{8(k+1)^2}{\left(3k \pm \sqrt{k\,(k-8)}\right)^2}\sqrt{\frac{k-2\pm\sqrt{k\,(k-8)}}{2\,(k+1)}}\sqrt{\frac{L}{C_{\text{eq}}}}. \tag{A4}$$

B. Derivation of Inductor Current Under Three Characteristic Roots

For "a simple root and two complex conjugate roots," "a simple root and two multiple roots," and "three simple roots," the general solutions of (6) are, respectively, as

$$i_L\,(t) = j_1 e^{r_1 t} + e^{\alpha t}\,(j_2\cos\beta t + j_3\sin\beta t) \tag{A5(a)}$$

$$i'_L\,(t) = j'_1 e^{r_1 t} + (j'_2 + j'_3 t)\,e^{\alpha t} \tag{A5(b)}$$

$$i''_L\,(t) = j''_1 e^{r_1 t} + j''_2 e^{r_2 t} + j''_3 e^{r_3 t} \tag{A5(c)}$$

where j_1, j_2, j_3, j'_1, j'_2, j'_3 and j''_1, j''_2, j''_3 are the coefficients, which will be determined afterwards.

For the three forms of characteristic roots, the final expression of v_{Cr}, i_{RC}, i_L, and v_{ds} are different. However, the detailed derivation processes are the similar. In this paper, the case of "a simple root and two complex conjugate roots" is given in detail.

It should be noted here that in a switching cycle, the *RC* snubber current i_{RC} is not zero at the initial stage of oscillation and the turning ON and OFF of switch will generates a sudden change of the current, while the voltage v_{Cr} of C_r is continuous. Therefore, at the *n*th number of switching cycle, when the switch is ON and OFF, v_{Cr} can be calculated as

$$v_{\text{Cr\_on}}\,(t) = v_{\text{Cr\_on\_initial}}\,(n)\cdot e^{-\frac{1}{R_r C_r}[t-(n-1)T_s]} \tag{A6}$$

$$v_{\text{Cr\_off}}\,(t) = V_o + [v_{\text{Cr\_on}}\,(T_{\text{on}}) - V_o]\,e^{-\frac{1}{R_r C_r}[t-(n-1)T_s-T_{\text{on}}]} \tag{A7}$$

where $v_{\mathrm{Cr\_on\_initial}}(n)$ is the initial value of v_{Cr} at the *n*th number of switching cycle, which can be calculated by (A27).

Based on (A7), the initial value of i_{RC} in the oscillation period at the *n*th number of switching cycle can be obtained as

$$\begin{aligned} i_{\mathrm{RC\_Td\_initial}}(n) &= C_r \frac{d}{dt} v_{\mathrm{Cr\_off}}(n,t)\Big|_{t=T_{\mathrm{off}}} \\ &= \frac{V_o - v_{\mathrm{Cr\_on}}(T_{\mathrm{on}})}{R_r} e^{-\frac{1}{R_r C_r} T_{\mathrm{off}}}. \end{aligned} \tag{A8}$$

Three initial conditions can be formulated as

$$\begin{cases} i_L|_{t=(n-1)T_s} = 0 \\ v_L|_{t=(n-1)T_s} = v_g(n) - V_o \\ i_{\mathrm{RC}}|_{t=(n-1)T_s} = i_{\mathrm{RC\_Td\_initial}}(n). \end{cases} \tag{A9}$$

According to (A9), the undetermined coefficients in A5(a) are calculated as, (A10) as shown at the bottom of this page.

Combining A5(a) with (A10), the inductor current i_L in the oscillation period at the *n*th number of switching cycle is expressed as

$$\begin{aligned} i_{L\_T_d}(t) = {} & \frac{1}{LC_{\mathrm{eq}}\beta\left(\beta^2 + (r_1-\alpha)^2\right)} \\ & \times \left(\left\{ \begin{bmatrix} i_{\mathrm{RC\_Td\_initial}}(n)(\alpha - r_1) \\ +C_{\mathrm{eq}}(v_g(n) - V_o)\left(\beta^2 + r_1^2 - \alpha^2\right) \end{bmatrix} \right. \right. \\ & \times \sin\left[\beta\left(t - (n-1)T_s - T_{\mathrm{on}} - T_{\mathrm{off}}\right)\right] \\ & + \left[2\alpha\beta C_{\mathrm{eq}}(v_g(n) - V_o) - \beta i_{\mathrm{RC\_Td\_initial}}(n)\right] \\ & \left. \left. \times \cos\left[\beta\left(t - (n-1)T_s - T_{\mathrm{on}} - T_{\mathrm{off}}\right)\right] \right\} \right. \\ & \times e^{\alpha \begin{bmatrix} t-(n-1)T_s \\ -T_{\mathrm{on}} - T_{\mathrm{off}} \end{bmatrix}} \\ & \left. - \begin{bmatrix} 2\alpha\beta C_{\mathrm{eq}}(v_g(n) - V_o) \\ -\beta i_{\mathrm{RC\_Td\_initial}}(n) \end{bmatrix} e^{r_1\left[t-(n-1)T_s - T_{\mathrm{on}} - T_{\mathrm{off}}\right]} \right) \end{aligned} \tag{A11}$$

where $(n-1)T_s + T_{\mathrm{on}} + T_{\mathrm{off}} \le t \le nT_s$.

Substituting (A11) into (4)–(5), the drain source voltage v_{ds} at the *n*th number of switching cycle is given by

$$\begin{aligned} v_{\mathrm{ds}\_T_d}(t) &= v_g(n) - L\frac{di_{L\_T_d}(t)}{dt} \\ &= v_g(n) - \frac{1}{\beta C_{\mathrm{eq}}\left(\beta^2 + (r_1-\alpha)^2\right)} \\ & \times \left(\left\{ \begin{bmatrix} i_{\mathrm{RC\_Td\_initial}}(n)\left[\alpha(\alpha - r_1) + \beta^2\right] \\ -\alpha C_{\mathrm{eq}}(v_g(n) - V_o)\left(\alpha^2 + \beta^2 - r_1^2\right) \end{bmatrix} \right. \right. \\ & \times \sin\left[\beta\left(t - (n-1)T_s - T_{\mathrm{on}} - T_{\mathrm{off}}\right)\right] \\ & \left. \left. -\beta \begin{bmatrix} r_1 i_{\mathrm{RC\_Td\_initial}}(n) \\ -C_{\mathrm{eq}}(v_g(n) - V_o)\left(\alpha^2 + \beta^2 + r_1^2\right) \end{bmatrix} \right\} \right. \\ & \times \cos\left[\beta\left(t - (n-1)T_s - T_{\mathrm{on}} - T_{\mathrm{off}}\right)\right] \\ & \times e^{\alpha \begin{bmatrix} t-(n-1)T_s \\ -T_{\mathrm{on}} - T_{\mathrm{off}} \end{bmatrix}} \\ & \left. + \beta \begin{bmatrix} i_{\mathrm{RC\_Td\_initial}}(n) \\ -2\alpha C_{\mathrm{eq}}(v_g(n) - V_o) \end{bmatrix} e^{r_1\left[t-(n-1)T_s - T_{\mathrm{on}} - T_{\mathrm{off}}\right]} \right) \end{aligned} \tag{A12}$$

where $(n-1)T_s + T_{\mathrm{on}} + T_{\mathrm{off}} \le t \le nT_s$.

Similarly, the *RC* snubber current i_{RC}, the voltage v_{Cr} of C_r, and the drain source current i_{ds} at the *n*th number of switching cycle can be calculated, respectively, as

$$\begin{aligned} i_{\mathrm{RC}\_T_d}(t) &= i_{L\_T_d}(t) + C_{\mathrm{eq}} L \frac{d^2 i_{L\_T_d}(t)}{d^2 t} \\ &= \frac{1}{LC_{\mathrm{eq}}\beta\left(\beta^2 + (r_1-\alpha)^2\right)} \\ & \times \left(\left\{ \begin{bmatrix} i_{\mathrm{RC\_Td\_initial}}(n) \begin{bmatrix} LC_{\mathrm{eq}} \begin{bmatrix} r_1\left(\beta^2 - \alpha^2\right) \\ +\alpha\left(\alpha^2 + \beta^2\right) \end{bmatrix} \\ +\alpha - r_1 \end{bmatrix} \\ +C_{\mathrm{eq}} \begin{pmatrix} V_o \\ -v_g(n) \end{pmatrix} \begin{bmatrix} LC_{\mathrm{eq}} \begin{bmatrix} \left(\alpha^2 + \beta^2\right)^2 \\ +r_1^2\left(\beta^2 - \alpha^2\right) \end{bmatrix} \\ +\alpha^2 - \beta^2 - r_1^2 \end{bmatrix} \end{bmatrix} \right. \right. \\ & \times \sin\left[\beta\left(t - (n-1)T_s - T_{\mathrm{on}} - T_{\mathrm{off}}\right)\right] \\ & + \beta \begin{bmatrix} i_{\mathrm{RC\_Td\_initial}}(n) \begin{bmatrix} LC_{\mathrm{eq}} \begin{pmatrix} \alpha^2 + \beta^2 \\ -2\alpha r_1 \end{pmatrix} - 1 \end{bmatrix} \\ +2\alpha C_{\mathrm{eq}}(v_g(n) - V_o)\left(LC_{\mathrm{eq}} r_1^2 + 1\right) \end{bmatrix} \\ & \left. \left. \times \cos\left[\beta\left(t - (n-1)T_s - T_{\mathrm{on}} - T_{\mathrm{off}}\right)\right] \right\} \right. \\ & \times e^{\alpha \begin{bmatrix} t-(n-1)T_s \\ -T_{\mathrm{on}} - T_{\mathrm{off}} \end{bmatrix}} \\ & \left. + \beta \begin{bmatrix} 2\alpha C_{\mathrm{eq}}(V_o - v_g(n)) \\ +i_{\mathrm{RC\_Td\_initial}}(n) \end{bmatrix} \left(LC_{\mathrm{eq}} r_1^2 + 1\right) \right. \\ & \left. \times e^{r_1\left[t-(n-1)T_s - T_{\mathrm{on}} - T_{\mathrm{off}}\right]} \right) \end{aligned} \tag{A13}$$

$$\begin{cases} j_1(n) = \dfrac{2\alpha C_{\mathrm{eq}}(V_o - v_g(n)) + i_{\mathrm{RC\_Td\_initial}}(n)}{LC_{\mathrm{eq}}\left(\alpha^2 + \beta^2 + r_1^2 - 2\alpha r_1\right)} \\ j_2(n) = \dfrac{2\alpha C_{\mathrm{eq}}(v_g(n) - V_o) - i_{\mathrm{RC\_Td\_initial}}(n)}{LC_{\mathrm{eq}}\left(\alpha^2 + \beta^2 + r_1^2 - 2\alpha r_1\right)} \\ j_3(n) = \dfrac{C_{\mathrm{eq}}\left(\alpha^2 - \beta^2 - r_1^2\right)(V_o - v_g(n)) + (\alpha - r_1) i_{\mathrm{RC\_Td\_initial}}(n)}{L\beta C_{\mathrm{eq}}\left(\alpha^2 + \beta^2 + r_1^2 - 2\alpha r_1\right)}. \end{cases} \tag{A10}$$

$$v_{\mathrm{Cr\_}T_d}(t)=v_{\mathrm{ds\_}T_d}(t)-R_r i_{\mathrm{RC\_}T_d}(t)=v_g(n)-\frac{1}{LC_{\mathrm{eq}}\beta\left(\beta^2+(r_1-\alpha)^2\right)}$$

$$\times\left(\begin{array}{l}\left\{\begin{array}{l}\left[\begin{array}{l}i_{\mathrm{RC\_Td\_initial}}(n)\left[\begin{array}{l}(\alpha L+R_r)(\alpha-r_1)\\+L\left[\begin{array}{l}\beta^2+C_{\mathrm{eq}}R_r\\\times\left[r_1\left(\beta^2-\alpha^2\right)+\alpha\left(\alpha^2+\beta^2\right)\right]\end{array}\right]\end{array}\right]\\+C_{\mathrm{eq}}\left(V_o-v_g(n)\right)\left[\begin{array}{l}LC_{\mathrm{eq}}R_r\times\\\left[\left(\alpha^2+\beta^2\right)^2+r_1^2\left(\beta^2-\alpha^2\right)\right]\\+(\alpha L+R_r)\left(\alpha^2-r_1^2\right)\\+(\alpha L-R_r)\beta^2\end{array}\right]\end{array}\right]\\\times\sin\left[\beta\left(t-(n-1)T_s-T_{\mathrm{on}}-T_{\mathrm{off}}\right)\right]\\+\beta\left[\begin{array}{l}C_{\mathrm{eq}}\left(v_g(n)-V_o\right)\left[\begin{array}{l}L\left(\alpha^2+\beta^2+r_1^2\right)\\+2\alpha R_r\left(LC_{\mathrm{eq}}r_1^2+1\right)\end{array}\right]\\+i_{\mathrm{RC\_Td\_initial}}(n)\\\times\left[R_r\left(LC_{\mathrm{eq}}\left(\alpha^2+\beta^2-2\alpha r_1\right)-1\right)-Lr_1\right]\end{array}\right]\\\times\cos\left[\beta\left(t-(n-1)T_s-T_{\mathrm{on}}-T_{\mathrm{off}}\right)\right]\end{array}\right\}e^{\alpha\left[\begin{smallmatrix}t-(n-1)T_s\\-T_{\mathrm{on}}-T_{\mathrm{off}}\end{smallmatrix}\right]}\\+\beta\left[\begin{array}{l}i_{\mathrm{RC\_Td\_initial}}(n)\left[L+R_r\left(LC_{\mathrm{eq}}r_1^2+1\right)\right]\\+2\alpha C_{\mathrm{eq}}\left(v_g(n)-V_o\right)\left[R_r\left(LC_{\mathrm{eq}}r_1^2+1\right)-L\right]\end{array}\right]e^{r_1\left[t-(n-1)T_s-T_{\mathrm{on}}-T_{\mathrm{off}}\right]}\end{array}\right)\tag{A14}$$

$$i_{\mathrm{ds\_}T_d}(t)=-C_{\mathrm{oss}}L\frac{d^2 i_{L\_T_d}(t)}{d^2t}=-\frac{C_{\mathrm{oss}}}{C_{\mathrm{eq}}\beta\left(\beta^2+(r_1-\alpha)^2\right)}$$

$$\times\left(\begin{array}{l}\left\{\begin{array}{l}\left[\begin{array}{l}i_{\mathrm{RC\_Td\_initial}}(n)\left[\begin{array}{l}r_1\left(\beta^2-\alpha^2\right)\\+\alpha\left(\alpha^2+\beta^2\right)\end{array}\right]\\+C_{\mathrm{eq}}\left(V_o-v_g(n)\right)\left[\begin{array}{l}\left(\alpha^2+\beta^2\right)^2\\+r_1^2\left(\beta^2-\alpha^2\right)\end{array}\right]\end{array}\right]\\\times\sin\left[\beta\left(t-(n-1)T_s-T_{\mathrm{on}}-T_{\mathrm{off}}\right)\right]\\+\beta\left[\begin{array}{l}i_{\mathrm{RC\_Td\_initial}}(n)\left(\alpha^2+\beta^2-2\alpha r_1\right)\\+2\alpha C_{\mathrm{eq}}r_1^2\left(v_g(n)-V_o\right)\end{array}\right]\\\times\cos\left[\beta\left(t-(n-1)T_s-T_{\mathrm{on}}-T_{\mathrm{off}}\right)\right]\end{array}\right\}e^{\alpha\left[\begin{smallmatrix}t-(n-1)T_s\\-T_{\mathrm{on}}-T_{\mathrm{off}}\end{smallmatrix}\right]}\\+\beta r_1^2\left[\begin{array}{l}2\alpha C_{\mathrm{eq}}\left(V_o-v_g(n)\right)\\+i_{\mathrm{RC\_Td\_initial}}(n)\end{array}\right]e^{r_1\left[t-(n-1)T_s-T_{\mathrm{on}}-T_{\mathrm{off}}\right]}\end{array}\right)\tag{A15}$$

where $(n-1)T_s+T_{\mathrm{on}}+T_{\mathrm{off}}\le t\le nT_s$.

Due to the effect of parasitic antiparallel diode on the switch, v_{ds} will be clamped at zero while it oscillates to zero. In a half line cycle, depending on whether v_{ds} can oscillate to zero or not, there are two situations about the inductor current. The cutoff point is the corresponding instantaneous input voltage, which enables the minimum value of v_{ds} to be just zero.

Obviously, when i_{ds} decreases to zero, v_{ds} is the minimum, and this time instant t_0 is the root of $i_{\mathrm{ds}}(t)=0$. Then, V_b can be obtained by defining $v_{\mathrm{ds}}(t_0)=0$. However, because of the complexity, it should be noted that there is no analytical expression of V_b. When $v_g(n)<V_b$, the oscillation current can be divided into three stages.

During the first stage T_{d1}, the inductor oscillates with the parasitic capacitor until v_{ds} decreases to zero, and the oscillation process is shown in Fig. 3(a). The expressions of i_{L_Td1}, $v_{\mathrm{ds\_}Td1}$, $i_{\mathrm{RC\_Td1}}$, and $v_{\mathrm{Cr\_}Td1}$ are the same as (A11)–(A14), where $(n-1)T_s+T_{\mathrm{on}}+T_{\mathrm{off}}\le t\le(n-1)T_s+T_{\mathrm{on}}+T_{\mathrm{off}}+T_{d1}$.

During the second stage T_{d2}, the body diode of the switch conducts. The inductor current and *RC* current decrease until the drain source current reaches zero. The oscillation process is

shown in Fig. 3(b), and the KVL equation is

$$\begin{cases} v_L(t) = v_g(n) \\ R_r \times i_{\mathrm{RC}}(t) + v_{C_r}(t) = 0. \end{cases} \tag{A16}$$

Two initial conditions of (A16) are expressed as

$$\begin{cases} i_L|_{t=(n-1)T_s+T_{\mathrm{on}}+T_{\mathrm{off}}+T_{d1}} \\ \quad = i_{L\_T_{d1}}\left((n-1)T_s + T_{\mathrm{on}} + T_{\mathrm{off}} + T_{d1}\right) \\ i_{\mathrm{RC}}|_{t=(n-1)T_s+T_{\mathrm{on}}+T_{\mathrm{off}}+T_{d1}} \\ \quad = i_{\mathrm{RC}\_T_{d1}}\left((n-1)T_s + T_{\mathrm{on}} + T_{\mathrm{off}} + T_{d1}\right). \end{cases} \tag{A17}$$

Based on (5) and (A16)–(A17), i_{L_Td2}, v_{ds_Td2}, $i_{\mathrm{RC\_Td2}}$, and v_{Cr_Td2} are derived as

$$i_{L\_T_{d2}}(t) = \begin{pmatrix} i_{L\_T_d}\left((n-1)T_s + T_{\mathrm{on}} + T_{\mathrm{off}} + T_{d1}\right) \\ + \dfrac{v_g(n)}{L}\left[t - (n-1)T_s - T_{\mathrm{on}} - T_{\mathrm{off}} - T_{d1}\right] \end{pmatrix} \tag{A18}$$

$$v_{\mathrm{ds}\_T_{d2}}(t) = 0 \tag{A19}$$

$$i_{\mathrm{RC}\_T_{d2}}(t) = \begin{pmatrix} i_{\mathrm{RC}\_T_d}\left((n-1)T_s + T_{\mathrm{on}} + T_{\mathrm{off}} + T_{d1}\right) \\ \times e^{-\frac{1}{R_r C_r}\left[t-(n-1)T_s - T_{\mathrm{on}} - T_{\mathrm{off}} - T_{d1}\right]} \end{pmatrix} \tag{A20}$$

$$v_{\mathrm{Cr}\_T_{d2}}(n,t) = \begin{pmatrix} v_{\mathrm{Cr}\_T_d}\left((n-1)T_s + T_{\mathrm{on}} + T_{\mathrm{off}} + T_{d1}\right) \\ \times e^{-\frac{1}{R_r C_r}\left[t-(n-1)T_s - T_{\mathrm{on}} - T_{\mathrm{off}} - T_{d1}\right]} \end{pmatrix} \tag{A21}$$

where $(n-1)T_s + T_{\mathrm{on}} + T_{\mathrm{off}} + T_{d1} \le t \le (n-1)T_s + T_{\mathrm{on}} + T_{\mathrm{off}} + T_{d1} + T_{d2}$.

During the third stage T_{d3}, the inductor and the equivalent parasitic capacitor oscillate until the time when the switch turns ON, and the oscillation process is plotted in Fig. 3(a).

Three initial conditions are formulated as

$$\begin{cases} i_L|_{t=(n-1)T_s+T_{\mathrm{on}}+T_{\mathrm{off}}+T_{d1}+T_{d2}} \\ \quad = i_{L\_T_{d2}}\begin{pmatrix} (n-1)T_s + T_{\mathrm{on}} \\ + T_{\mathrm{off}} + T_{d1} + T_{d2} \end{pmatrix} \\ v_L|_{t=(n-1)T_s+T_{\mathrm{on}}+T_{\mathrm{off}}+T_{d1}+T_{d2}} = v_g(n) \\ i_{\mathrm{RC}}|_{t=(n-1)T_s+T_{\mathrm{on}}+T_{\mathrm{off}}+T_{d1}+T_{d2}} \\ \quad = i_{\mathrm{RC}\_T_{d2}}\begin{pmatrix} (n-1)T_s + T_{\mathrm{on}} \\ + T_{\mathrm{off}} + T_{d1} + T_{d2} \end{pmatrix}. \end{cases} \tag{A22}$$

i_{L_Td3}, v_{ds_Td3}, $i_{\mathrm{RC\_Td3}}$, and v_{Cr_Td3} can be obtained as

$$\begin{aligned} i_{L\_T_{d3}}(t) = {} & \frac{1}{L\beta\left(\beta^2 + (r_1-\alpha)^2\right)} \\ & \times \left(\begin{cases} \begin{bmatrix} \left(\beta^2 + r_1^2 - \alpha^2\right) v_g(n) \\ + \left(\alpha^2 - \beta^2 - \alpha r_1\right) L r_1 i_{L\_T_{d3}\_\mathrm{initial}}(n) \end{bmatrix} \times \\ \sin\left[\beta\begin{pmatrix} t-(n-1)T_s - T_{\mathrm{on}} \\ -T_{\mathrm{off}} - T_{d1} - T_{d2} \end{pmatrix}\right] \\ + \begin{bmatrix} 2\alpha\beta v_g(n) \\ + (r_1 - 2\alpha) L\beta r_1 i_{L\_T_{d3}\_\mathrm{initial}}(n) \end{bmatrix} \\ \times \cos\left[\beta\begin{pmatrix} t-(n-1)T_s - T_{\mathrm{on}} \\ -T_{\mathrm{off}} - T_{d1} - T_{d2} \end{pmatrix}\right] \end{cases} \right. \\ & \times e^{\alpha\begin{bmatrix} t-(n-1)T_s - T_{\mathrm{on}} \\ -T_{\mathrm{off}} - T_{d1} - T_{d2} \end{bmatrix}} \\ & - \left[\left(\alpha^2 + \beta^2\right) L i_{L\_T_{d3}\_\mathrm{initial}}(n) - 2\alpha v_g(n)\right] \\ & \left. \times e^{r_1\begin{bmatrix} t-(n-1)T_s - T_{\mathrm{on}} \\ -T_{\mathrm{off}} - T_{d1} - T_{d2} \end{bmatrix}} \right) \end{aligned} \tag{A23}$$

$$\begin{aligned} v_{\mathrm{ds}\_T_{d3}}(t) = {} & v_g(n) - \frac{1}{\beta\left(\beta^2 + (r_1-\alpha)^2\right)} \\ & \times \left(\begin{cases} \begin{bmatrix} \alpha\left(r_1^2 - \alpha^2 - \beta^2\right) v_g(n) \\ + L r_1\left(\alpha^2 + \beta^2\right)(\alpha - r_1) i_{L\_T_{d3}\_\mathrm{initial}}(n) \end{bmatrix} \times \\ \sin\left[\beta\begin{pmatrix} t-(n-1)T_s - T_{\mathrm{on}} \\ -T_{\mathrm{off}} - T_{d1} - T_{d2} \end{pmatrix}\right] \\ + \beta\begin{bmatrix} \left(\alpha^2 + \beta^2 + r_1^2\right) v_g(n) \\ - L r_1\left(\alpha^2 + \beta^2\right) i_{L\_T_{d3}\_\mathrm{initial}}(n) \end{bmatrix} \\ \times \cos\left[\beta\begin{pmatrix} t-(n-1)T_s - T_{\mathrm{on}} \\ -T_{\mathrm{off}} - T_{d1} - T_{d2} \end{pmatrix}\right] \end{cases} \right. \\ & \times e^{\alpha\begin{bmatrix} t-(n-1)T_s - T_{\mathrm{on}} \\ -T_{\mathrm{off}} - T_{d1} - T_{d2} \end{bmatrix}} \\ & + \beta r_1\begin{bmatrix} L\left(\alpha^2 + \beta^2\right) i_{L\_T_{d3}\_\mathrm{initial}}(n) \\ -2\alpha v_g(n) \end{bmatrix} \\ & \left. \times e^{r_1\begin{bmatrix} t-(n-1)T_s - T_{\mathrm{on}} \\ -T_{\mathrm{off}} - T_{d1} - T_{d2} \end{bmatrix}} \right) \end{aligned} \tag{A24}$$

$$i_{\mathrm{RC}\_T_{d3}}(t) = i_{L\_T_{d3}}(t) + C_n L\frac{d^2 i_{L\_T_{d3}}(t)}{d^2 t} \tag{A25}$$

$$v_{\mathrm{Cr}\_T_{d3}}(t) = v_{\mathrm{ds}\_T_{d3}}(t) + R_r i_{\mathrm{RC}\_T_{d3}}(t) \tag{A26}$$

where $(n-1)T_s + T_{\mathrm{on}} + T_{\mathrm{off}} + T_{d1} + T_{d2} \le t \le nT_s$, $i_{L\_Td3\_\mathrm{initial}}(n)$ is the initial value of i_L in T_{d3}, which is given in (A22). Here it should be pointed out that the expressions of $i_{\mathrm{RC\_Td3}}(t)$ and $v_{\mathrm{Cr}\_Td3}(t)$ are too long to be completely demonstrated.

According to (A25)–(A26), $v_{\mathrm{Cr\_on\_initial}}(n)$ can be figured out as, eq. (27) as shown at the top of next page.

$$v_{\mathrm{Cr\_on\_initial}}(n)=\begin{cases} v_{\mathrm{Cr}\_T_{d1}}\left((n-2)T_s+T_{\mathrm{on}}+T_{\mathrm{off}}+T_d\right),\ v_g(n-1)\geq V_b \\ v_{\mathrm{Cr}\_T_{d1}}\left((n-2)T_s+T_{\mathrm{on}}+T_{\mathrm{off}}+T_d\right),\ v_g(n-1)<V_b\ \&\ T_d\leq T_{d1} \\ v_{\mathrm{Cr}\_T_{d2}}\left((n-2)T_s+T_{\mathrm{on}}+T_{\mathrm{off}}+T_d\right),\ v_g(n-1)<V_b\ \&\ T_{d1}<T_d\leq T_{d1}+T_{d2} \\ v_{\mathrm{Cr}\_T_{d3}}\left((n-2)T_s+T_{\mathrm{on}}+T_{\mathrm{off}}+T_d\right),\ v_g(n-1)<V_b\ \&\ T_d>T_{d1}+T_{d2}. \end{cases} \tag{A27}$$

REFERENCES

[1] H. Bodur and S. Yıldırmaz, "A new ZVT snubber cell for PWM-PFC boost converter," *IEEE Trans. Ind. Electron.*, vol. 64, no. 1, pp. 300–309, Jan. 2017.

[2] C. Zhao, J. Zhang, and X. Wu, "An improved variable on-time control strategy for a CRM flyback PFC converter," *IEEE Trans. Power Electron.*, vol. 32, no. 2, pp. 915–919, Feb. 2017.

[3] A. Leon-Masich, H. Valderrama-Blavi, J. M. Bosque-Moncusí, and L. Martínez-Salamero, "A high-voltage SiC-based boost PFC for LED applications," *IEEE Trans. Power Electron.*, vol. 31, no. 2, pp. 1633–1642, Feb. 2016.

[4] J. W. Kim and G. W. Moon, "Minimizing effect of input filter capacitor in a digital boundary conduction mode power factor corrector based on time-domain analysis," *IEEE Trans. Power Electron.*, vol. 31, no. 5, pp. 3827–3836, May 2016.

[5] Y. Chen and Y. Chen, "Line current distortion compensation for DCM/CRM boost PFC converters," *IEEE Trans. Power Electron.*, vol. 31, no. 3, pp. 2026–2038, Mar. 2016.

[6] J. W. Kim, H. S. Youn, and G. W. Moon, "A digitally controlled critical mode boost power factor corrector with optimized additional on time and reduced circulating losses," *IEEE Trans. Power Electron.*, vol. 30, no. 6, pp. 3447–3456, Jun. 2015.

[7] B. Zhao, A. Abramovitz, and K. Smedley, "Family of bridgeless buck-boost PFC rectifiers," *IEEE Trans. Power Electron.*, vol. 30, no. 12, pp. 6524–6527, Dec. 2015.

[8] A. Kessal and L. Rahmani, "Ga-optimized parameters of sliding-mode controller based on both output voltage and input current with an application in the PFC of AC/DC converters," *IEEE Trans. Power Electron.*, vol. 29, no. 6, pp. 3159–3165, Jun. 2014.

[9] V. M. Lopez, F. J. Azcondo, A. de Castro, and R. Zane, "Universal digital controller for boost CCM power factor correction stages based on current rebuilding concept," *IEEE Trans. Power Electron.*, vol. 29, no. 7, pp. 3818–3829, Jul. 2014.

[10] B. A. Mather and D. Maksimović, "A simple digital power-factor correction rectifier controller," *IEEE Trans. Power Electron.*, vol. 26, no. 1, pp. 9–19, Jan. 2011.

[11] J. Han, B. Zhang, and D. Qiu, "Bi-switching status modeling method for DC-DC converters in CCM and DCM operations," *IEEE Trans. Power Electron.*, vol. 32, no. 3, pp. 2464–2472, Mar. 2017.

[12] J. H. Yi, W. Choi, and B. H. Cho, "Zero-voltage-transition interleaved boost converter with an auxiliary coupled inductor," *IEEE Trans. Power Electron.*, vol. 32, no. 8, pp. 5917–5930, Aug. 2017.

[13] C. Cheng, C. Chang, T. Chung, and F. Yang, "Design and implementation of a single-stage driver for supplying an LED street-lighting module with power factor corrections," *IEEE Trans. Power Electron.*, vol. 30, no. 2, pp. 956–966, Feb. 2015.

[14] K. Yao, W. Hu, Q. Li, and J. Lyu, "A novel control scheme of DCM boost PFC converter," *IEEE Trans. Power Electron.*, vol. 30, no. 10, pp. 5605–5615, Oct. 2015.

[15] K. Yao, X. Ruan, X. Mao, and Z. Ye, "Variable-duty-cycle control to achieve high input power factor for DCM boost PFC converter," *IEEE Trans. Ind. Electron.*, vol. 58, no. 5, pp. 1856–1865, May 2011.

[16] X. Zhang and J. W. Spencer, "Analysis of boost PFC converters operating in the discontinuous conduction mode," *IEEE Trans. Power Electron.*, vol. 26, no. 12, pp. 3621–3628, Dec. 2011.

[17] H. S. Athab, "A duty cycle control technique for elimination of line current harmonics in single-stage DCM boost PFC circuit," in *Proc. IEEE Region 10 Conf.*, 2008, pp. 1–6.

[18] Z. Ye and M. M. Jovanovic, "Implementation and performance evaluation of DSP-based control for constant-frequency discontinuous-conduction-mode boost PFC front end," *IEEE Trans. Ind. Electron.*, vol. 52, no. 1, pp. 98–107, Feb. 2005.

[19] R. Fernandes and O. Trescases, "A multimode 1-MHz PFC front end with digital peak current modulation," *IEEE Trans. Power Electron.*, vol. 31, no. 8, pp. 5694–5708, Aug. 2016.

[20] H. S. Youn, J. B. Lee, J. I. Baek, and G. W. Moon, "A digital phase leading filter current compensation (PLFCC) technique for CCM boost PFC converter to improve PF in high line voltage and light load conditions," *IEEE Trans. Power Electron.*, vol. 31, no. 9, pp. 6596–6606, Sep. 2016.

[21] Q. Ji, X. Ruan, L. Xie, and Z. Ye, "Conducted EMI spectra of average-current-controlled boost PFC converters operating in both CCM and DCM," *IEEE Trans. Ind. Electron.*, vol. 62, no. 4, pp. 2184–2194, Apr. 2015.

[22] C. W. Clark, F. Musavi, and W. Eberle, "Digital DCM detection and mixed conduction mode control for boost PFC converters," *IEEE Trans. Power Electron.*, vol. 29, no. 1, pp. 347–354, Jan. 2014.

[23] S. Moon, L. Corradini, and D. Maksimovic, "Autotuning of digitally controlled boost power factor correction rectifiers," *IEEE Trans. Power Electron.*, vol. 26, no. 10, pp. 3006–3018, Oct. 2011.

[24] L. Roggia, F. Beltrame, J. E. Baggio, and J. R. Pinheiro, "Digital control system applied to a boost PFC converter operating in mixed conduction mode," in *Proc. Brazilian Power Electron. Conf.*, 2009, pp. 698–704.

[25] K. De Gusseme, D. M. Van de Sype, A. P. M. Van den Bossche, and J. A. Melkebeek, "Digitally controlled boost power-factor-correction converters operating in both continuous and discontinuous conduction mode," *IEEE Trans. Ind. Electron.*, vol. 52, no. 1, pp. 88–97, Feb. 2005.

[26] R. K. Tripathi, S. P. Das, and G. K. Dubey, "Mixed mode operation of boost switch-mode rectifier for wide range of load variations," *IEEE Trans. Power Electron.*, vol. 17, no. 6, pp. 999–1009, Nov. 2002.

[27] J. Sebastian, J. A. Cobos, J. M. Lopera, and J. Uceda, "The determination of the boundaries between continuous and discontinuous conduction modes in PWM DC-to-DC converters used as power factor preregulators," *IEEE Trans. Power Electron.*, vol. 10, no. 1, pp. 574–582, Sep. 1995.

[28] R. Redl, "Reducing distortion in boost rectifiers with automatic control," in *Proc. IEEE Appl. Power Electron. Conf.*, 1997, pp. 74–80.

[29] L. Huber, B. T. Irving, and M. M. Jovanovic, "Effect of valley switching and switching-frequency limitation on line-current distortions of DCM/CCM boundary boost PFC converters," *IEEE Trans. Power Electron.*, vol. 24, no. 2, pp. 339–347, Feb. 2009.

[30] F. Xiong, J. Zhang, and Z. Qian, "Effect of parasitic parameters on current distortion of boost PFC circuit," *Proc. CSEE*, vol. 30, no. 21, pp. 40–47, Jul. 2010.

[31] F. Z. Chen and D. Maksimović, "Digital control for improved efficiency and reduced harmonic distortion over wide load range in boost PFC rectifiers," *IEEE Trans. Power Electron.*, vol. 25, no. 10, pp. 2683–2692, Oct. 2010.

[32] S. W. Lee and H. L. Do, "Single-stage bridgeless AC-DC PFC converter using a lossless passive snubber and valley switching," *IEEE Trans. Ind. Electron.*, vol. 63, no. 10, pp. 6055–6063, Oct. 2016.

[33] M. Li, B. Zhang, D. Qiu, and G. Zhang, "Sneak circuit phenomena in a DCM boost converter considering parasitic parameters," *IEEE Trans. Power Electron.*, vol. 32, no. 5, pp. 3946–3958, May 2017.

[34] K. Harada, T. Ninomiya, and M. Kohno, "Optimum design of an RC snubber for a switching regulator by means of the root locus method," in *Proc. IEEE Power Electron. Spec. Conf.*, 1978, pp. 158–167.

[35] K. De Gusseme, D. M. Van de Sype, A. P. M. Van den Bossche, and J. A. Melkebeek, "Input current distortion of CCM boost PFC converters operated in DCM," *IEEE Trans. Ind. Electron.*, vol. 54, no. 2, pp. 858–865, Apr. 2007.

[36] Q. Li, K. Yao, J. Song, H. Xu, and Y. Han, "A series diode method of suppressing parasitic oscillation for boost PFC converter operated in discontinuous conduction mode," *IEEE Trans. Power Electron.*, vol. 33, no. 1, pp. 407–424, Jan. 2018.

[37] G. Cardano and T. R. Witmer, *Ars Magna or The Rules of Algebra*. New York, NY, USA: Dover, 1993.

[38] Cubic Function, 2018. [Online]. Available: https://en.wikipedia.org/wiki/Cubic_function.

[39] Multiplicity of a root of a polynomial, 2018. [Online]. Available: https://en.m.wikipedia.org/wiki/Multiplicity_(mathematics)#Multiplicity_of_a_root_of_a_polynomial

Kai Yao (M'14) was born in Jiangsu Province, China, in 1980. He received the B.S. degree in industrial automation from Nantong University, Nantong, China, the M.S. degree in mechanical design and theory, and Ph.D. degree in electrical engineering from Nanjing University of Aeronautics and Astronautics, Nanjing, China, in 2002, 2005, and 2010, respectively.

In 2011, he joined the Faculty of Electrical Engineering, School of Automation, Nanjing University of Science and Technology, where he has been engaged in teaching and research in the field of power electronics. His main research interests include power factor correction converters, condition monitoring, and diagnostics of power converters.

Hairui Xu was born in Jiangsu Province, China, in 1992. He received the B.S. degree in electrical engineering and automation from Nanjing University of Science and Technology, Nanjing, China, in 2015. He is currently working toward the M.S. degree in power electronics and electric drives with Nanjing University of Science and Technology.

His research interest focuses on power factor correction converters.

Qiang Li was born in Jiangsu Province, China, in 1969. He received the B.S. degree in automatic control from Harbin Institute of Technology, Harbin, China, and the Ph.D. degree in electrical engineering from Southeast University, Nanjing, China, in 1992 and 2005, respectively.

In 2005, he joined the Faculty of Electrical Engineering, School of Automation, Nanjing University of Science and Technology, where he has been engaged in teaching and research in the field of electrical engineering. His main research interests include electric machine design, control and drive for electrical machine, switching mode power supply, and embedded system.

Yehua Han was born in Jiangsu Province, China, in 1991. He received the B.S. degree in electrical engineering and automation from Nanjing University of Science and Technology, Nanjing, China, in 2015. He is currently working toward the M.S. degree in power electronics and electric drives with Nanjing University of Science and Technology.

His research interest focuses on power factor correction converters.

Ke Yun was born in Inner Mongolia Autonomous Region, China, in 1993. He received the B.S. degree in electrical engineering and automation from Nanjing University of Science and Technology, Nanjing, China, in 2016. He is currently working toward the M.S. degree in electrical engineering from Nanjing University of Science and Technology.

His research interest focuses on power factor correction converters.